Remote Sensing of Environment 260 (2021) 112440

Contents lists available at ScienceDirect

Remote Sensing of Environment

journal homepage: www.elsevier.com/locate/rse

The effect of pixel heterogeneity for remote sensing based retrievals of evapotranspiration in a semi-arid tree-grass ecosystem

Vicente Burchard-Levine [a,*], Héctor Nieto [b], David Riaño [a,c], Mirco Migliavacca [d], Tarek S. El-Madany [d], Radoslaw Guzinski [e], Arnaud Carrara [f], M. Pilar Martín [a]

[a] Environmental Remote Sensing and Spectroscopy Laboratory (SpecLab), Spanish National Research Council (CSIC), 28037 Madrid, Spain
[b] Complutum Tecnologías de la Información Geográfica S.L. (COMPLUTIG), Alcalá de Henares, Madrid, Spain
[c] Center for Spatial Technologies and Remote Sensing (CSTARS), University of California, 139 Veihmeyer Hall, One Shields Avenue, Davis, CA 95616,USA
[d] Max Planck Institute for Biogeochemistry, Department Biogeochemical Integration, Hans-Knöll-Str. 10, D-07745 Jena, Germany
[e] DHI GRAS, Agern Alle 5, Hørsholm 2970, Denmark
[f] Fundación Centro de Estudios Ambientales del Mediterráneo (CEAM), 46980 Paterna, Spain

ARTICLE INFO

Keywords:
Evapotranspiration
Latent heat flux
Sensible heat flux
Tree-grass ecosystems
Surface energy balance
Spatial resolution
Airborne imagery
Sentinels for evapotranspiration
Land surface temperature

ABSTRACT

Many satellite missions rely on modeling approaches to acquire global or regional evapotranspiration (ET) products. However, a current challenge in ET modeling lies in dealing with sub-pixel heterogeneity, as models often assume homogeneous conditions at the pixel level. This is particularly an issue for heterogeneous landscapes, such as tree-grass ecosystems (TGE). In these areas, while appearing homogeneous at larger spatial scales pertaining to a single land cover type, the separation of the spectral signals of the main landscape features (e.g. trees and grasses) may not be achieved at the conventional satellite sensor resolution (e.g. 10–1000 m). This leads to important heterogeneity within the pixel grid that may not be accounted for in traditional modeling frameworks. This study examined the effect of pixel heterogeneity on ET simulations over a complex TGE in central Spain. High resolution hyperspectral imagery from five airborne campaigns forced the two-source energy balance (TSEB) model at 1.5–1000 m spatial resolutions. Along with this, the sharpened (20 m) and original (1000 m) Sentinels for Evapotranspiration (Sen-ET) products were evaluated over the study site for 2017. Results indicated that TSEB accurately simulated ET (RMSD: ~60 W/m^2) when the pixel scale was able to robustly discriminate between grass and tree pixels (<5 m). However, model uncertainty drastically increased at spatial resolution greater than 10 m (RMSD: ~115 W/m^2). Model performance remains relatively constant between 30 and 1000 m spatial resolutions, with within pixel heterogeneity being similar at all these scales. For mixed pixels (≥30 m), forcing an effective landscape roughness into TSEB (RMSD: ~80 W/m^2) or applying a seasonally changing TSEB (TSEB-2S; RMSD: ~65 W/m^2) improved the modeling performance. The Sen-ET products behaved similarly at both scales with RMSD of ET roughly 80 W/m^2. The non-linear relationship between input parameters and flux output, along with the poor representation of aerodynamic surface roughness, were the main drivers for the increased uncertainties at coarser scales. These results suggest that care should be taken when using global ET products over TGE and similarly heterogeneous landscapes. The modeling procedure should inherently account for the presence of vastly different vegetation roughness elements within the pixel, to achieve reliable estimates of turbulent fluxes over a TGE.

1. Introduction

Three major groups of methods have been proposed to retrieve evapotranspiration (ET) from remote sensing data (Kustas and Anderson, 2009; Li et al., 2017; Mu et al., 2011) (1) empirical approaches that either upscale point measurements to gridded data using vegetation indices (VI) and meteorological data (e.g. Jung et al., 2019, 2009) or are based on the relationship between VI and land surface

* Corresponding author.
E-mail addresses: vicentefelipe.burchard@cchs.csic.es (V. Burchard-Levine), hector.nieto@complutig.com (H. Nieto), david.riano@cchs.csic.es (D. Riaño), mmiglia@bgc-jena.mpg.de (M. Migliavacca), telmad@bgc-jena.mpg.de (T.S. El-Madany), rmgu@dhigroup.com (R. Guzinski), arnaud@ceam.es (A. Carrara), mpilar.martin@cchs.csic.es (M.P. Martín).

https://doi.org/10.1016/j.rse.2021.112440
Received 9 May 2020; Received in revised form 15 January 2021; Accepted 4 April 2021
Available online 19 April 2021

temperature (LST) (e.g. Gillies et al., 1997; Nishida et al., 2003); (2) traditional methods such as Penman-Monteith (PM) or Priestley-Taylor (PT) approaches combined with optical remote sensing and weather data inputs (e.g. Mu et al., 2011) including those merging them with soil water balance schemes (e.g. Bastiaanssen et al., 2012; Hu and Jia, 2015; Martens et al., 2017); and (3) surface energy balance (SEB) models that exploit both thermal infrared (TIR) and optical regions to solve ET through the radiation and energy balance equations (e.g. Allen et al., 2007; Norman et al., 1995; Su, 2002; Xu et al., 2019).

SEB models find a good compromise between being physically-based without the need for extensive data inputs and parameters (Kustas and Anderson, 2009). This makes them particularly suited for applications at different spatial scales since they rely less on locally constrained data (Anderson et al., 2003). SEB models obtain ET as the residual of the energy balance, where the available energy (AE), defined as net radiation (Rn) minus ground heat flux (G), is partitioned between sensible heat (H) and latent heat (LE) (i.e. ET) fluxes. However, SEB models must address the aerodynamic-radiometric temperature difference, which for semi-arid and/or sparse vegetation can be up to several degrees different (Colaizzi et al., 2004; Norman et al., 1995). Single-source SEB models treat the surface as a single composite layer. They require a method to relate the remotely sensed radiometric temperature with that of the aerodynamic temperature. These are often based on the use of an additional resistance term that accounts for the various factors affecting the radiometric-aerodynamic temperature difference (Kustas et al., 2016). This may include accounting for the difference between the roughness length for heat transport (z_{0H}) and the roughness length for momentum transport (z_{0M}). z_{0M} and z_{0H} tend to be largely different as they are affected by different processes, such as the turbulent drag on roughness elements for momentum and the molecular diffusion near the surface for heat transport (Jia, 2004; Verhoef et al., 1997). The differences between the two are usually defined through the kB^{-1} parameter, which is often difficult to estimate without large parameterizations (Boulet et al., 2015). Although, the widely used Surface Energy Balance System (SEBS) (Su, 2002) proposed a method to determine kB^{-1} through remote sensing derived parameters such as LAI and vegetation fractional cover.

Other SEB schemes, through a 'two-source' approach, tackle this issue by separating the surface temperature and energy exchange into vegetation and soil components while considering the directional effects of the TIR observations (Anderson et al., 1997; Boulet et al., 2015; Norman et al., 2003, 1995). As these models consider soil and vegetation separately, this approach explicitly accommodates for the major differences between radiometric and aerodynamic temperature. Vegetation cover and the sensor viewing geometry most notably affect this temperature difference (Kustas et al., 2016; Norman et al., 1995). The two-source energy balance (TSEB) model (Norman et al., 1995) applies this rationale. Compared to one-source models, TSEB provides a more physical depiction of water and energy fluxes' processes (Boulet et al., 2015). This avoids the need for additional empirical terms or depending on certain conditions being met (e.g. presence of hot and cold pixels; e.g. Allen et al. (2007)) within the region of interest (ROI). Adaptations to the TSEB modeling framework were implemented in Kustas and Norman (1999) to better represent partial canopy cover conditions and past studies demonstrated that TSEB provided reliable flux estimates for clumped and partially vegetated landscapes under water-limited conditions (Burchard-Levine et al., 2020; Kustas et al., 2019, 2016; Li et al., 2019; Song et al., 2018; Timmermans et al., 2007).

Many satellite missions rely on modeling approaches for global ET products. These include ESA's Sentinel constellation, which recently published the Sentinels for ET (Sen-ET) product (Guzinski et al., 2020) and NASA's ECOsystem Spaceborne Thermal Radiometer Experiment on Space Station (ECOSTRESS) mission (Fisher et al., 2020). However, there are many scaling issues that must be considered when modeling the surface-atmosphere exchanges (Anderson et al., 2003; Brunsell and Gillies, 2003; Moran et al., 1997). A current challenge in regional and global flux modeling lies in dealing with sub-pixel heterogeneity. Different land covers, vegetation and surface properties all contribute to the sensor signal and to the mass and energy exchange. It thus becomes an issue to adequately characterize a heterogenous grid with a single parameter value, especially since models typically assume both vertically and horizontally homogenous canopies. The influence of spatial resolution on ET retrievals derived from modeling methods has been discussed in a number of studies (Ershadi et al., 2013; Kustas et al., 2004; Kustas and Norman, 2000; Lagouarde et al., 2015, 2013; McCabe and Wood, 2006; Moran et al., 1997; Nassar et al., 2020). Among them, a common approach is to resample the remote sensing-based inputs to quantify the model uncertainty at different scales. For example, Moran et al. (1997) demonstrated that the site heterogeneity highly influenced the errors in turbulent heat flux estimations from the aggregation of remote sensing inputs. The largest errors in H were associated to sites with important variations in aerodynamic roughness with patchy vegetation, especially for more unstable conditions. While Lagouarde et al. (2015, 2013) showed an increased spatio-temporal variability of surface temperatures at finer spatial resolutions. This was related to the surface boundary-layer turbulence, which could potentially induce larger errors in very high resolution LST measurements and flux estimates.

Landscapes with complex vegetation canopies, even usually classified under a singular land cover type, have different structural traits that may hinder the applicability of conventional models and remote sensing techniques. For example, tree-grass ecosystems (TGE), savanna-like landscapes with scattered isolated trees coexisting (while superimposing) over a rather continuous grass understory, have inherently complex structural features. This causes for important surface variability and heterogeneity at small scales, presenting clear difficulties for Earth observation and modeling methods (e.g. Andreu et al., 2018; Cleugh et al., 2007; Whitley et al., 2017), even though at larger spatial scales these landscapes appear homogeneous. Remote sensing-based SEB models tend to have greater uncertainty in TGEs, with adaptations needed to obtain reliable flux estimates (e.g. Andreu et al., 2018; Burchard-Levine et al., 2020). As discussed in Whitley et al. (2017), traditional land surface models have greater uncertainties in savanna ecosystems due to the co-dominant structural features of the trees and grass and their differentiated phenology. While tree density over the grass understory are relatively homogeneously distributed within these landscapes, important small-scale horizontal and vertical spatial heterogeneities are present, coupled with strong differences in the seasonal contribution of the different vegetation layers to total fluxes (Burchard-Levine et al., 2020; El-Madany et al., 2020; Luo et al., 2018). This is an important gap since these ecosystems are not only important in extent (~15% of the global surface) but savannas and other semi-arid ecosystems were highlighted in recent studies (e.g. Ahlström et al., 2015; Biederman et al., 2017; Jung et al., 2011) for their important role in the global biogeochemical cycle, being the main contributor to the variability of global carbon and water fluxes.

In these ecosystems, the separation of the spectral signals of the main landscape features (e.g. trees, grasses and/or shrubs) may not be achieved from the currently available satellite spatial resolution (e.g. 10–1000 m). Under this hypothesis, this work addressed heterogeneity and scale issues in relation to the accuracy of turbulent flux exchange modeling due to variability in land surface biophysical properties and aerodynamic roughness, which characterize savanna-like ecosystems. With this objective, high-resolution hyperspectral imagery from five airborne campaigns quantified the uncertainty in flux retrievals over a complex TGE for 1.5–1000 m pixel sizes. These spatial scales were designed to mimic the sensor spatial resolution of the main satellite missions currently available. Three different model parameterization strategies accounted for vegetation mixing at the pixel level: a weighted averaging approach, a seasonally changing TSEB assumption (i.e. TSEB-2S, Burchard-Levine et al., 2020) and forcing effective roughness parameter values into TSEB. The 20 and 1000 m Sen-ET products (Guzinski et al., 2020) were also evaluated to contextualize this analysis.

2. Methods

2.1. Study site and in-situ measurements

The study was conducted in the TGE experimental site Majadas de Tiétar (39°56′24.68″N, 5°46′28.70″W) in central Spain (Casals et al., 2009; El-Madany et al., 2018). TGE are both prevalent in the Iberian Peninsula (known as *'dehesa'* in Spain and *'montado'* in Portugal) and globally extensive, covering nearly 15% of total Earth surface (Friedl et al., 2010). These ecosystems have important ecological (i.e. biodiversity and carbon stock) and economic (i.e. livestock grazing) roles (Moreno and Pulido, 2008). However, traditional remote sensing methods tend to have greater uncertainty in these complex landscapes (Andreu et al., 2018; Burchard-Levine et al., 2020; Giri et al., 2005; Melendo-Vega et al., 2018). The study site is a managed semi-natural agroforested area with scattered evergreen broadleaf trees, mostly Holm Oak (*Quercus ilex* L.) superimposing a nearly continuous grass understory. The fractional tree canopy cover at the site is 19.7 ± 4.9% (El-Madany et al., 2020). The grass layer is mostly composed of annual species from three plant functional groups: grasses, forbs and legumes (Migliavacca et al., 2017). It lies within a continental Mediterranean climate region with very hot and dry summer periods (~June to September), with the grass rapidly drying and senescing during these conditions. The area averages 16.7 °C annual temperature and about 650 mm annual precipitation, with significant inter-annual variability (Luo et al., 2018). Between 2015 and 2018, August was the hottest and driest month reaching mean ~ 31 °C temperatures and ~11 mm of rainfall. January was the coldest month with average ~ 9 °C temperature, while October was, on average, the wettest month with ~98 mm of rainfall.

Three EC towers operate simultaneously within the experimental site since 2014. They are located relatively close to each other (<650 m, Fig. 1), with similar tree fractional cover (f_c) within their footprint, but belong to a large-scale nutrients manipulation experiment (El-Madany et al., 2018). Nitrogen was added to the northern tower (NT, FLUXNET ID ES-LM1), nitrogen and phosphorus to the southern tower (NPT, FLUXNET ID ES-LM2) and the central tower was kept as a control (CT, FLUXNET ID ES-LMa). The EC systems are identical for all three towers, consisting of a three-dimensional sonic anemometer (R3–50, Gill LTD UK) and an infrared gas analyzer (LI-7200, Licor Bioscience, Lincoln, USA) at a measurement height of 15 m, about 7 m above the tree canopy. A four–component net radiometer (CNR4, Kipp and Zonen, Delft, Netherlands) measures both shortwave and longwave incoming and outgoing radiation at roughly 15 m above ground. The weighted average of eight soil heat flux plates, buried at a depth of 5 cm, represent ecosystem scale soil heat flux (G) and was calculated for each treatment individually. They were located both in open grass and below tree canopy and weighted to consider shadow effects throughout the day. Note that corrections related to heat storage above the soil heat flux plates were not applied. Measurements of Rn, H, LE and G from the tower systems served to benchmark model performance. The average energy balance closure ratio (i.e. [LE + H]/[Rn - G]) for each tower ranged from 0.74 to 0.79 during the overpasses of the airborne acquisitions used in this study (Table 1). The EC energy balance closure issue is an underlying uncertainty in SEB studies using these data, with the main causes for this lack of closure, as well as potential corrections, still under debate (e.g. Foken et al., 2011; Stoy et al., 2013). Since TSEB closes the energy balance by definition, allocating the residuals to the observed LE, ensured this closure assuming that errors in LE are larger than H. This was shown valid for this site in Perez-Priego et al. (2017) with independent LE estimates. Additionally, similar studies applied the same strategy (e.g. Burchard-Levine et al., 2020; Guzinski et al., 2014; Kustas et al., 2012). Along with this, auxiliary meteorological measurements from the towers forced the TSEB model. These included incoming shortwave irradiance (SW_{in}), incoming longwave irradiance (LW_{in}), air temperature (T_a), relative humidity (RH), and wind speed (u), all measured at a height of 15 m above ground level. These tower measurements were considered to be describing meteorological conditions at the ecosystem scale and were maintained spatially consistent across the ROI. Refer to El-Madany et al. (2018) for more details on the

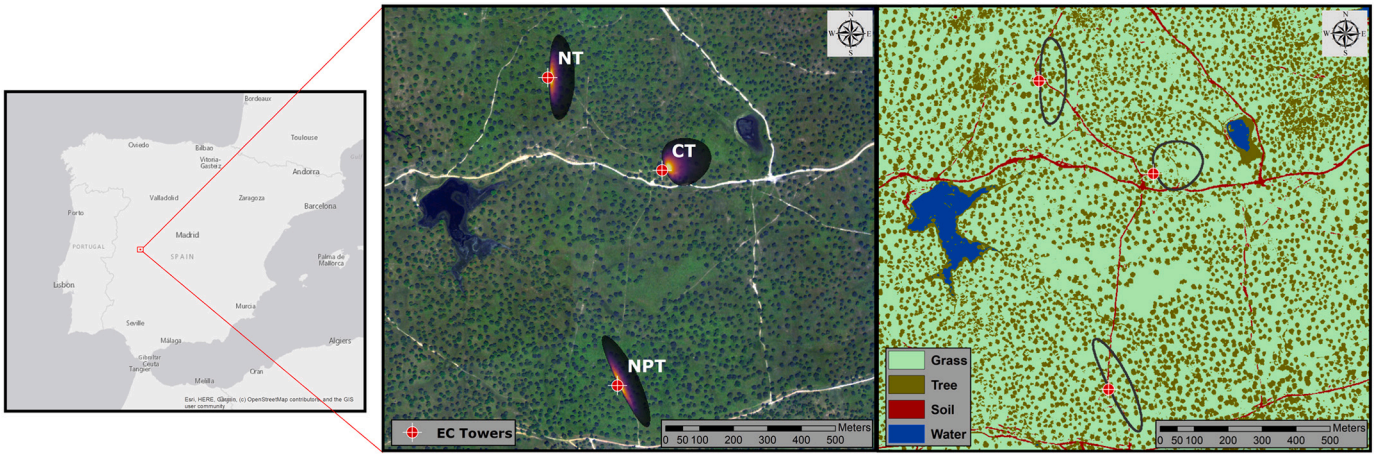

Fig. 1. Study site location with the three EC towers (red points), along with land cover map. The ROI true colour image was acquired from the CASI airborne image mosaic of 2014-04-08 and tower footprints were estimating according to Kljun et al. (2015). (For interpretation of the references to colour in this figure legend, the reader is referred to the web version of this article.)

Table 1
Date, time, and meteorological conditions during the AHS overpasses.

Date	Time (UTC)	Ta (°C)	SW_{in} (Wm^{-2})	u ($m\ s^{-1}$)	RH (%)	Mean NDVI of ROI (−)
2014-04-08	11:47	22.04	859.58	1.63	60.14	0.65
2015-04-23	12:15	21.56	939.55	2.96	43.07	0.61
2015-07-03	12:05	32.16	944.98	1.36	32.73	0.37
2016-05-03	12:15	23.89	968.86	3.76	31.65	0.64
2017-05-19	12:17	21.18	982.28	1.07	36.31	0.48

instrumentation and flux calculation procedures. Ground measurements of leaf area index (LAI) for individual trees were acquired using the LAI-2200 plant canopy analyzer (LAI-2200) (LICOR Bioscience USA, 2011) over five campaigns at different seasonal periods between 2017 and 2018. Each campaign measured twelve trees distributed over two sampling plots. The average local tree LAI ranges between 1.39 and 1.75 m^2/m^2 (~0.35 m^2/m^2 effective LAI) and has low inter-annual variability (Luo et al., 2018). In-situ destructive grass LAI (both green and total LAI), along with proximal spectral measurements, were also acquired from 15 field campaigns between 2017-03-16 and 2019-06-12. Field protocols are described in Mendiguren et al. (2015) and Melendo-Vega et al. (2018). These ground measurements created empirical models between reflectance factors and grass biophysical variables (see Section 2.3.2).

2.2. Remote sensing airborne data

This study processed five high spatial resolution airborne hyperspectral images acquired over the Majadas experimental site (Table 1). The Spanish National Institute for Aerospace Technology (INTA) operated these flights using two sensors: the Compact Airborne Spectrographic Imager (CASI-1500i; Itres Research Ltd., Canada) and the Airborne Hyperspectal Scanner (AHS). The CASI (i.e. CASI-1500i) is a pushbroom imaging spectrometer with 144 spectral bands within the visible and near-infrared (VNIR) regions (i.e. 0.38 and 1.05 μm) with a field of view (FOV) of ~40° and ground spatial resolution of 1.5 m (after resampling) at 1839 m above ground level. Spectral bands were atmospherically corrected using ATCOR-4™ (ReSe Applications GmbH, Germany) to derive top-of-canopy reflectance (de Miguel et al., 2015). The AHS sensor has 63 bands in the VNIR and shortwave infrared regions (0.43 to 2.55 μm), 7 bands in the middle infrared (3.3 to 5.4 μm) and 10 bands in the TIR region (i.e. 8 and 13 μm) with a FOV of ~90°. The adjusted normalized emissivity method (ANEM) retrieved LST from the AHS TIR bands (Coll et al., 2003, 2001) within ATCOR-4™ (de Miguel et al., 2015) with an average output spatial resolution of 4.5 m. For each campaign, the selection of the North-South AHS overpass centered in the EC towers and closest to solar noon were selected to limit solar and angular effects. Since the CASI imagery swath width is narrower compared to the AHS sensor, mosaics of several overpasses obtained an image that overlapped all the three tower footprints (Pacheco-Labrador et al., 2020).

2.3. ET retrievals using the Two-Source Energy Balance (TSEB) model

2.3.1. Model overview

The TSEB model, described in Norman et al. (1995) and Kustas and Norman (1999), was applied in the Majadas experimental site. TSEB estimates LE (i.e. ET) as the residual of the surface energy balance. It considers that the combined emission of both soil and vegetation components compose the total temperature emitted by the bulk surface. This is weighted by the fraction of vegetation observed by the sensor (Eq. (1)).

$$\boldsymbol{LST}(\boldsymbol{\theta}) = \left[\boldsymbol{f}(\boldsymbol{\theta})\boldsymbol{T}_c^4 + (\mathbf{1} - \boldsymbol{f}(\boldsymbol{\theta}))\boldsymbol{T}_s^4\right]^{1/4} \quad (1)$$

where $f(\theta)$ is the fraction of vegetation observed by the TIR sensor at an angle θ and is mainly a function of LAI; T_c is the vegetation canopy temperature (K); and T_s is the soil surface temperature (K). LST is the main boundary condition in TSEB, serving as a proxy of soil moisture, both a near-surface through soil evaporation and root-zone through canopy transpiration, together with vegetation condition. Through Eq. (1), LST is separated into vegetation (T_c) and soil (T_s) temperature and the energy balance is decoupled for the two separate layers (Eqs. (2)–(3)).

$$\boldsymbol{R}_{N,c} = \boldsymbol{LE}_c + \boldsymbol{H}_c \quad (2)$$

$$\boldsymbol{R}_{N,s} = \boldsymbol{LE}_s + \boldsymbol{H}_s + \boldsymbol{G} \quad (3)$$

where R_N is the net radiation (W m^{-2}), LE is latent heat flux (W m^{-2}), H is sensible heat flux (W m^{-2}), G is the soil heat flux (W m^{-2}), and subscripts s and c refer to soil and vegetation canopy sources, respectively. Radiative transfer and absorption through the canopy ($R_{N,c}$ and $R_{N,s}$) are simulated using an extinction coefficient approach, primarily dictated by the amount of canopy foliage (i.e. LAI) and architecture (i.e. X_{LAD}), along with the incident solar angle, as described in chapter 15 of Campbell and Norman (1998). This radiative transfer model separates incoming shortwave irradiance between direct (i.e. beam) and diffused radiation along with separating between VIS (400–700 nm) and NIR (700–2500 nm) spectral regions, since reflectivity and transmissivity change drastically between vegetation and soil features (Campbell and Norman, 1998). LW radiation transfer is modeled similarly but only considering diffused radiation from the TIR region. For more details, the reader is referred to chapter 15 of Campbell and Norman (1998) or to the source code (https://github.com/hectornieto/pyTSEB/blob/master/pyTSEB/net_radiation.py#L546).

H is then estimated for both soil and vegetation sources, assuming both layers interact with each other and with the atmosphere, using their respective temperatures (Eqs. (4)–(6)).

$$\boldsymbol{H}_s = \frac{\boldsymbol{\rho c_p}(\boldsymbol{T}_s - \boldsymbol{T}_{AC})}{\boldsymbol{R}_S} \quad (4)$$

$$\boldsymbol{H}_c = \frac{\boldsymbol{\rho c_p}(\boldsymbol{T}_c - \boldsymbol{T}_{AC})}{\boldsymbol{R}_X} \quad (5)$$

$$\boldsymbol{H} = \boldsymbol{H}_s + \boldsymbol{H}_c = \frac{\boldsymbol{\rho c_p}(\boldsymbol{T}_{AC} - \boldsymbol{T}_A)}{\boldsymbol{R}_A} \quad (6)$$

where T_{AC} is the air temperature within the canopy space (K) and is equivalent to the aerodynamic temperature (K); R_A is the aerodynamic resistance to heat transfer based on the Monin-Obukhov similarity theory and is estimated as (Kustas et al., 2016):

$$\boldsymbol{R}_A = \frac{ln\left[\left(\frac{\boldsymbol{z_u - d0}}{\boldsymbol{z_{0M}}} - \boldsymbol{\Psi m}\right)\right]\left[ln\left(\frac{\boldsymbol{z_t - d0}}{\boldsymbol{z_{0M}}} - \boldsymbol{\Psi h}\right)\right]}{\boldsymbol{k^2 u}} \quad (7)$$

where z_u (m) and z_t (m) are measurement heights for wind speed and air temperature, respectively; d0 the zero-plane displacement height (m); z_{0M} the roughness length for momentum transfer (m); k is the von Karman's constant (0.4); and Ψm and Ψh are the Monin-Obukhov atmospheric stability functions for momentum and heat, respectively. R_S, the resistance to heat transfer in the boundary layer above soil layer (s m^{-1}), is computed as:

$$\boldsymbol{R}_S = \frac{\mathbf{1}}{\boldsymbol{c}(\boldsymbol{T}_s - \boldsymbol{T}_c)^{1/3} + \boldsymbol{bu}_s} \quad (8)$$

where u_s is the wind speed just above the surface where the impact of soil roughness is minimal (i.e., $z_{0,\ soil}$); b (−) and c ($s^{1/2}$ m^{-1}) are coefficients taken from Kustas and Norman (1999) and Norman et al. (1995). These are based on the works of Sauer and Norman (1995) and Kondo and Ishida (1997). The wind speed above the surface (at height $z_{0,\ soil}$) is estimated from the tower measurement at 15 m that is extrapolated below the canopy using the Goudriaan (1977) exponential wind attenuation law (Eq. (9)).

$$u_{z0soil} = u_c exp\left(-a\left(1 - \left(\frac{z0soil}{h_c}\right)\right)\right) \quad (9)$$

where u_c is the wind speed top of canopy (m s^{-1}), h_c is the canopy height (m) and $a = 0.28\mathrm{LAI}^{2/3}h_c{}^{1/3}l_w^{1/3}$ where l_w is the effective leaf width size (m).

R_X, the bulk canopy resistance to heat transfer (s m^{-1}), is estimated

Table 2
Parameter values for the grass-soil and tree-soil cover model configurations.

Parameters	Description	Tree-soil	Grass-soil	Source
α_{PT} (−)	Priestley Taylor coefficient (−)	1.26	1.26	Norman et al. (1995)
f_c (−)	Fractional cover (−)	0.2	1	El-Madany et al. (2018)
w_c (−)	Canopy width to height ratio (−)	1	1	Pacheco-Labrador et al. (2017)
X_{LAD} (−)	Leaf inclination distribution parameter (−)	1	1	Campbell and Norman (1998)
h_c (m)	Canopy height (m)	8	0.5	El-Madany et al. (2018)
$z0_{soil}$ (m)	Bare soil aerodynamic roughness length (m)	0.01	0.01	Norman et al. (1995)
l_w (m)	Effective leaf width (m)	0.05	0.01	Guzinski et al. (2014); Norman et al. (1995)
b (−)	Soil-surface resistance (Rs) coefficient (−)	0.034	0.012	Sauer and Norman (1995)
c (m s^{-1} $K^{-1/3}$)	Soil-surface resistance (Rs) coefficient (m s^{-1} $K^{-1/3}$)	0.0025	0.0025	Kondo and Ishida (1997)
C′ ($s^{1/2}$ m^{-1})	Total boundary resistance (Rx) constant ($s^{1/2}$ m^{-1})	90	90	McNaughton and Van Den Hurk (1995)

as:

$$R_X = \frac{C' \sqrt{l_w / u_{d_o+z_{0m}}}}{LAI} \tag{10}$$

where u_{d0+z0m} is the wind speed within the canopy-air interspace at the height of momentum source/sink (m s^{-1}); and C′ ($s^{1/2}$ m^{-1}) is a coefficients taken from Kustas and Norman (1999) based on McNaughton and Van Den Hurk (1995) (see Table 2 for all values used). T_{AC} is solved using the 'series' approach, which assumes the vegetation and soil are fully coupled (i.e. 'layered' model). The component temperature of each source (T_s and T_c) along with aerodynamic resistances (R_A, R_S, and R_X) interact to influence the estimated within-canopy temperature, T_{AC} (equivalent in TSEB to the aerodynamic temperature). For more details on this approach, the reader is referred to Appendix A in Norman et al. (1995). Since T_s and T_c are unknown a priori, an iterative process is applied, initially assuming that the photosynthetically active part of the vegetation (i.e. through f_g, the fraction of LAI that is green) is transpiring at a potential rate based on the Pristley-Taylor formulation (Eq. (11)).

$$LE_{ci} = \alpha_{PT} f_g \left(\frac{\Delta}{\Delta + \gamma}\right) R_{N,c} \tag{11}$$

where LE_{ci} is the initial canopy transpiration estimate (W m^{-2}); α_{PT} is the Priestley-Taylor coefficient (default is 1.26) (−), defined in this case only for the canopy source; Δ is the slope of the saturation vapor pressure curve at air temperature T_A (kPa K^{-1}); and γ is the psychrometric constant (kPa K^{-1}). The canopy transpiration is subsequently reduced until realistic fluxes are achieved ($LE_c \geq 0$ and $LE_s \geq 0$). For more details regarding the TSEB model, refer to Norman et al. (1995), Kustas and Norman (1999) or the python implementation (pyTSEB) (https://github.com/hectornieto/pyTSEB).

Burchard-Levine et al. (2020) proposed a two-season modeling approach with TSEB (TSEB-2S) to account for phenological dynamics present in semi-arid TGE. This strategy divides the annual simulation periods into two main phenological seasons within TGEs: a grass dominated (grass-soil) growing period and a tree dominated (tree-soil) summer drought period. An asymmetric gaussian filter over a normalized difference vegetation index (NDVI) time series from MODIS (MCD43A4 product) estimated the seasonal transition dates between the growing and summer seasons. The summer drought begins when NDVI starts to decay at the downward inflection point (beginning of grass senescence) of the gaussian fit and ends when NDVI reaches the upward inflection point (re-greening). The assumption of a different dominant vegetation cover allows different model parameterizations between the two major phenological periods. This strategy improved the use of a two-source representation (i.e. TSEB) for an essentially three source (i.e. tree-grass-soil) TGE site, using the combination of proximal TIR data and satellite based VI (Burchard-Levine et al., 2020). Table 2 shows the parameter values of the two different modeling periods in TSEB-2S. As shown in Table 2, it should be noted that the grass f_c is 1 and maintained constant throughout the simulation period, since the grass rather homogeneously covers the entire soil surface even during the dry period. Nevertheless, the f_g derived from remote sensing data (Section 2.3.2) dictates the percentage of grass that is photosynthetically active and is highly seasonal. To clarify, f_c is different to $f(\theta)$ from eq.1 as f_c mostly characterizes the clumping distribution of the vegetation, while $f(\theta)$, a function of LAI and sensor viewing angle, partitions the temperature contribution from vegetation and soil sources.

In addition to the different parameter sets, each season employs a different method to estimate the roughness parameters, d0 and z_{0M}. When considering the grass-soil system during the growing period, the traditional fixed ratio to canopy height (i.e. $d0 = 0.65h_c$; $z_{0M} = 0.125h_c$) was used (Campbell and Norman, 1998). The Raupach (1994) model was applied for the tree-soil representation during the summer drought period when grass is fully dry. The latter method considers the canopy shape and density (e.g. LAI, f_c) effect on roughness and is generally accepted as more appropriate for tall, wooded vegetation. For this study, the airborne overpasses of 2015-07-03 and 2017-05-19 were within the tree-soil dry/summer period, while all the other overpasses (i.e. 2014-04-08, 2015-04-23, and 2016-05-03) were part of the grass-soil growing period (Fig. A6).

2.3.2. Retrievals of vegetation biophysical variables for model inputs

Land cover classification (LCC) and biophysical variables required by TSEB were retrieved at 1.5 m spatial resolution using reflectance measurements from the CASI sensor. A LCC map was produced for each overpass date by supervised classification of the CASI images based on the Mahalanobis distance (Richards and Jia, 2006). Image pixels were classified as trees, grass, water, or bare soil (shadow pixels were masked out). A look-up table was linked to the LCC map to assign surface parameters that were not directly retrieved through remote sensing methods (e.g. h_c, l_w; see Table 2).

Empirical models from destructive in-situ LAI (total and green) measurements and hyperspectral data acquired on the ground from an ASD Fieldspec3 spectroradiometer derived grass LAI and f_g. A total of 186 samples were acquired in 15 field campaigns between 2017-03-16 and 2019-06-12 within the context of the SynerTGE project (http://www.lineas.cchs.csic.es/synertge/). The dataset was separated randomly in subsets to train (60%) and validate (40%) the model. The partial least square regression (PLSR) method was applied using the ASD spectra (resampled to mimic the 136 CASI bands between 400 and 1005 nm) as the predictor variables (X) to estimate LAI and green LAI (LAIg) (Y). Five PLSR components were used, which resulted in an R^2 of 0.78 and 0.82 with the validation subset for LAI and LAIg, respectively (see Figs. A1 and A2). The empirical model was then applied with the CASI reflectance factors of the grass pixels to retrieve LAI and f_g (defined as LAIg/LAI) for the five airborne campaigns over the study site. For tree pixels, constant LAI (~1.75m^2m^{-2}) and f_g (0.9) were assumed according to field measurements (Section 2.1), considering relatively low spatial variability of the Oak tree structure within the ROI.

2.3.3. Thermal sharpening

Numerous ET modeling studies have applied thermal sharpening algorithms to maximize the temporal and spatial resolutions of different

satellite sensors (e.g. Anderson et al., 2011; Guzinski et al., 2020; Ma et al., 2018). In this study, this was incorporated to better separate the thermal signal between tree and grass pixels. As described in Gao et al. (2012), the Data Mining Sharpener (DMS) generated an LST product at the same spatial resolution as the vegetation products derived from the CASI sensor (i.e. 1.5 m). The DMS applies a machine-learning algorithm that derives a statistical relationship between the coarser resolution variable (i.e. LST) and the finer resolution variable (i.e. VNIR reflectance), aggregated to the scale of the coarse resolution variable (Fig. 2). Assuming that the relation is consistent at varying spatial scales, the DMS algorithm uses the native high resolution (i.e. VNIR reflectance) data as independent variables to derive a sharpened or disaggregated representation of the coarse resolution variable (i.e. LST). In this study, the DMS is implemented using an artificial neural network (ANN) fitting method (https://github.com/radosuav/pyDMS/). The ANN is first trained with samples composed of CASI pixels that are relatively homogeneous at the AHS pixel level. Pixel homogeneity is quantified by the coefficient of variation of fine resolution pixels located within the extent of a coarse resolution pixel. Pixels are added to the training sample if the sub-pixel variation (i.e. coefficient of variation) at the CASI resolution scale is less than 20%. The statistical relationships are performed on both the local (using a moving window of 15 × 15 pixels at the AHS scale) and global level (using the entire ROI). In addition, residual analysis and bias corrections are applied to maintain consistency (i.e. conservation of energy of longwave radiation) between sharpened/disaggregated pixels and their corresponding original AHS pixel. For more details, refer to Gao et al. (2012), Guzinski and Nieto (2019), Guzinski et al. (2020) or to the source code which is freely available via https://github.com/radosuav/pyDMS/.

2.3.4. Mutli-scale ET retrievals and evaluation

The principal model run simulated fluxes at 1.5 m spatial resolution using CASI derived biophysical variables (Section 2.3.2) and a sharpened LST based on the AHS sensor (Section 2.3.3). Along with this configuration, input data (LST and biophysical variables) were resampled at five other spatial scales to investigate the effect of pixel size on modeled fluxes. The pixel sizes tested were: 4.5 m (original AHS), 10 m (Sentinel-2 MSI-Like), 30 m (Landsat8 OLI-like), 100 m (Landsat8 TIR-like) and 1000 m (MODIS and Sentinel-3 SLTSR-like). The biophysical products (i.e. f_g and LAI) were resampled from the original 1.5 m CASI-based products using linear averaging, while the LST product was resampled based on the original 4.5 m AHS LST retrieval, aggregating the average thermal radiance emission (Fig. 3). This approach uses the best possible biophysical product derived from the native resolution and, by using linear averaging and maintaining mean values, it limits the uncertainties in the model performance associated to the changes and uncertainty between radiances and biophysical products. This way, it can more clearly pinpoint the effect of spatial scale on the model uncertainty related to the model structure and parameterization. For the model runs at 1.5, 4.5 and 10 m spatial resolution, tree and grass pixels were distinguishable and different parameter sets were assigned based on vegetation cover classification (Table 2, except f_c for trees was kept at 1.0 assuming, at these scales, the whole pixel was vegetated). Since turbulent exchange occurs at plant or even at larger scales, trees were treated as objects by only selecting the center-most pixels within the tree crown (i.e. those pixels more than 3 m distance from the grass pixels) and assigning the mean values of those pixels to the whole tree crown. This was done to limit edge/boundary effects of the trees. As pixels at the edge of the tree crown may be affected by the adjacent grass (and/or other land cover) signals, this may induce artificial boundary effects, especially if the tree and grass temperatures are very different.

The high-resolution data were used here as 'benchmark runs' to simulate the fluxes the best way possible as, at this spatial scale, different parameter values can be assigned for tree and grass pixels. For coarser model runs (i.e. at 30 m, 100 m and 1000 m), the separation of the multiple vegetation sources (i.e. trees and grasses) was not possible at the pixel scale. Therefore, parameters inherently needed to be adjusted at effective values to consider these mixed conditions. In this study, three different strategies were tested to adjust the parameter values to characterize the single, mixed, vegetation source as assumed in TSEB: 1) averaging and weighting vegetation parameters (e.g. h_c and l_w) based on the fractional cover of trees and grasses at each pixel as derived from the CASI LCC, 2) applying TSEB-2S, which changes the parameterization assumption for different seasons (Section 2.3.1; Table 2) and 3) forcing consistent landscape-level roughness values for all spatial scales. For the latter, an effective landscape roughness was estimated and incorporated for all grid sizes assessed, maintaining the same model configuration for all model runs from 1.5 m to 1000 m, as suggested by Hopwood (1996) and Mahrt (1993). As such, the parameterization was the same for tree and grass pixels, even for high resolution (i.e. <10 m) model runs. The roughness parameters (i.e. d0 and z_{0M}) were directly forced into TSEB instead of being estimated within the model based on the inputs/parameters (i.e. h_c, f_c, and LAI). Landscape d0 and z_{0M} were calculated using the Raupach (1994) model, under the assumption that the scattered trees are the main roughness elements. In the study site, the spatial distribution of these roughness elements over the surface

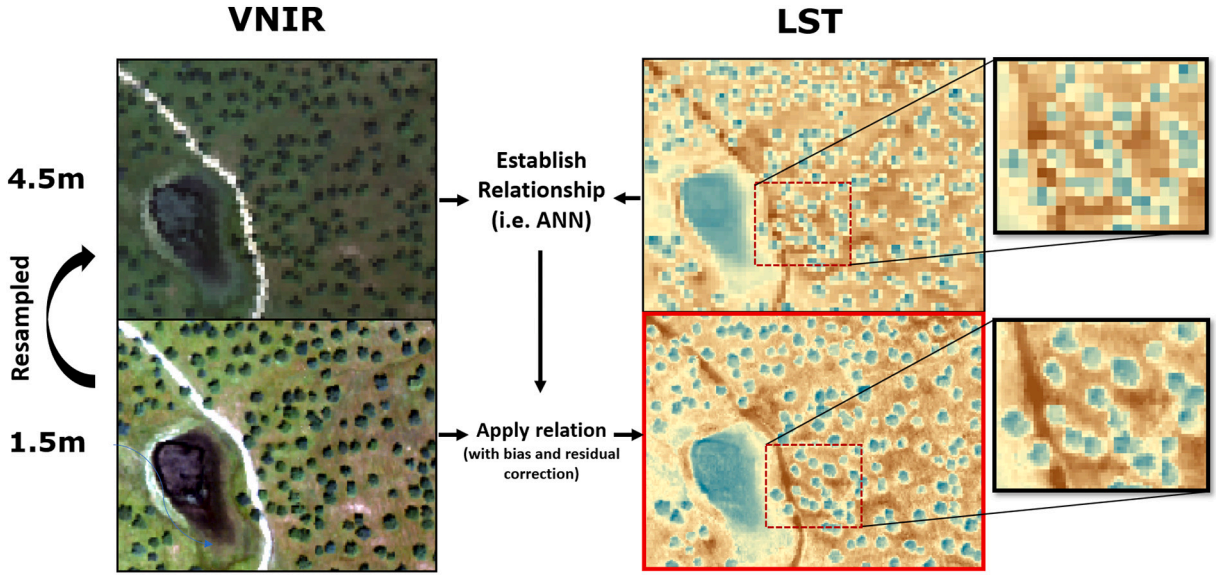

Fig. 2. Scheme of thermal sharpening with DMS algorithm to sharpen AHS LST (right) with the CASI VNIR bands (left).

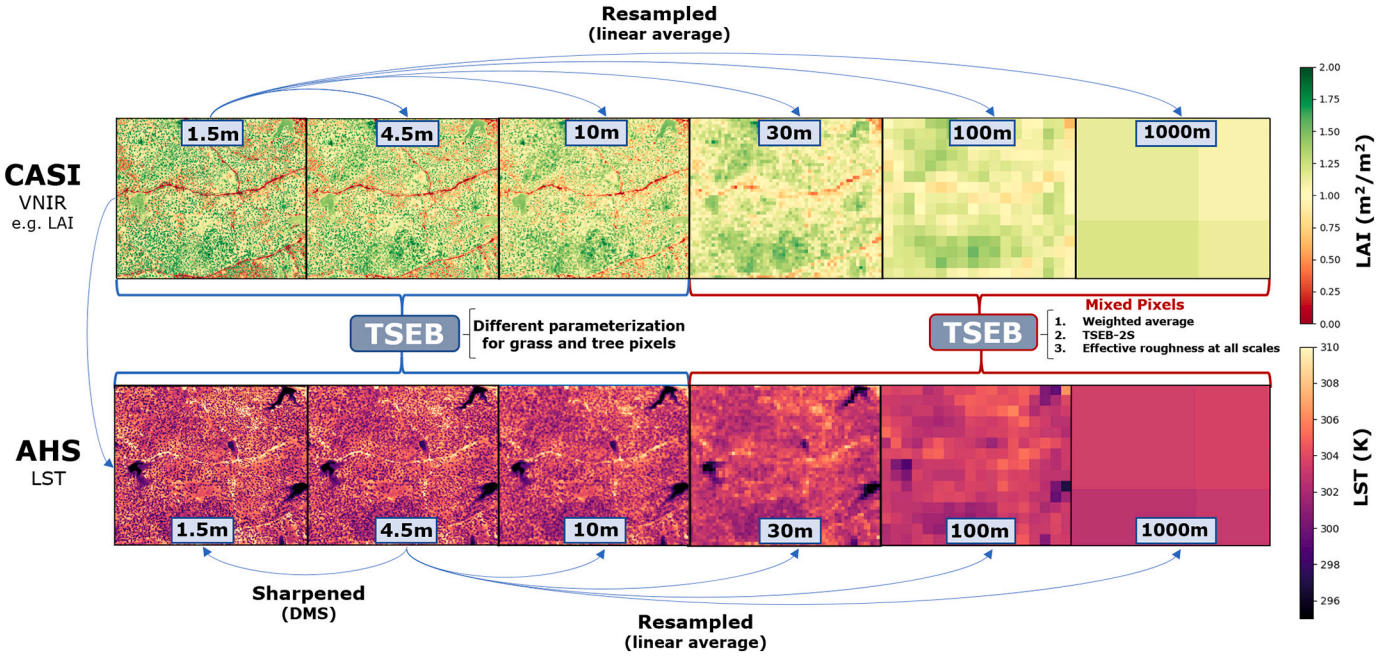

Fig. 3. General model set up and parameterization for the different scales assessed (1.5 m – 1000 m) using airborne imagery from the 2016-05-03 12:15UTC acquisition as an example.

remains relatively constant across scales. It is only at the 1000 m pixel scale, that the pixel grid includes more heterogeneous elements such as water and/or bare soil (this is further discussed below in Section 4). An h_c of 8 m, f_c of 0.2 and a local tree LAI of 1.75 m^2/m^2 (effective LAI = 0.35 m^2/m^2) yielded a z_{0M} and d_0 of 0.60 m and 4.04 m, respectively. All spatial scales assessed (i.e. 1.5–1000 m) applied these effective roughness values, while keeping the standard values (i.e. grass-soil configuration in Table 2) for the other parameters.

Three EC tower measurements located within the study site evaluated the model results. The mean of the instantaneous modeled fluxes (LE, H, Rn and G) of all pixels located within the tower footprint, weighted by the normalized footprint probability density function (PDF), was compared against the corresponding EC-based measurements. The two-dimensional tower footprints were estimated based on Kljun et al. (2015) during the time step of the image acquisition, where the PDF was normalized through its integral. Modeled fluxes, at all spatial resolutions, were resampled to 1.5 m and then weighted with the corresponding pixel of the normalized PDF footprint. Additionally, to better compare the results from the set of acquisitions at different overpass times, the modeled evaporative fraction (EF) (i.e. LE/(Rn-G)) was also assessed. It should be noted that due to missing G data during the 2014-04-08 overpass, observed LE could not be corrected for energy balance closure using the same method as the other dates. Therefore, the model performance evaluation omitted these data points. Meaning that for the 2014-04-08 overpass, only Rn and H are assessed. Model performance was evaluated with the root-mean-square-deviation (RMSD, Eq. (12)), mean bias (Eq. (13)) and the Pearson's correlation coefficient (r).

$$\mathrm{RMSD} = \sqrt{\frac{\sum (Y_{TSEB} - Y_{EC})^2}{N}} \tag{12}$$

$$bias = \frac{\sum (Y_{TSEB} - Y_{EC})}{N} \tag{13}$$

where Y_{TSEB} is mean modeled flux (LE, H, Rn or G) over the tower footprint; Y_{EC} is the observed EC flux (LE, H, Rn or G); and N is the total number of observations.

2.4. Sen-ET product

The Sen-ET product (Guzinski et al., 2020) used the same modeling method (i.e. TSEB) and provides energy flux products at both 20 m and 1000 m spatial resolution. Therefore, it was evaluated to contextualize the above analysis. A plug-in for the SNAP software (http://step.esa.int/main/toolboxes/snap/) was developed using open global datasets: Sentinel-2 MSI VNIR data, Seninel-3 SLSTR TIR data, meteorological data from ECMWF ERA-5 reanalysis dataset (available from the Copernicus Climate Data Store: https://cds.climate.copernicus.eu) and a landcover map (for assigning values to parameters listed in Table 2) from ESA CCI 2015 land cover product (Bontemps et al., 2013). The 20 m products sharpen LST derived from the DMS algorithm (Guzinski et al., 2020; Guzinski and Nieto, 2019). For more information on this product, refer to the user manual (User Manual for Sen-ET SNAP Plugin v.1.0, 2019) and to Guzinski et al. (2020). Sen-ET products were processed for the entire year of 2017. Overpasses over the ROI with cloud cover and Sentinel-3 SLSTR viewing zenith angle greater than 45 degrees were discarded. A total of 106 products at each of the spatial resolutions were processed for the year 2017 (ranging from DOY 7 to 358). The flux outputs were evaluated against the EC data for the three tower footprints (at the time step of Sentinel-3 overpass times).

In addition, the Sen-ET product was compared to the local airborne acquisition from 2017-05-19, providing a spatial evaluation of the Sen-ET methodology. This was the only airborne overpass available matching the Sen-ET temporal period. Since the temporally nearest Sentinel-2 MSI images were cloudy, Landsat-8 OLI multispectral data (30 m) from 2017-05-16 was used instead and fluxes were retrieved following the Sen-ET methodology. The Sentinel-3 Level 2 LST product from 2017-05-19 (overpass at ~10:25 UTC) was sharpened to 30 m using the VNIR band information from the Landsat-8 acquisition. The same method as the airborne simulations retrieved LAI and f_g (Section 2.3.2.). The Sen-ET procedure assigned the other parameters, as seen in Table 2 and described in Guzinski et al. (2020). The earliest AHS airborne overpass (i.e. 11:08) from 2017-05-19 (resampled to 30 m) was compared against this sharpened Sen-ET(−like) 30 m product of the same date.

3. Results

3.1. High resolution modeled fluxes (1.5 m)

The TSEB model was applied at 1.5 m spatial resolution using the sharpened LST product (Section 2.3.3) and biophysical variables derived from the CASI sensor (Section 2.3.2). Fig. 4 shows the spatial and temporal distribution of LE within the ROI for the five airborne overpasses. Mean LE within the entire ROI (ignoring water and soil pixels) for the individual overpasses ranged from 295 to 493 W m^{-2}, or in relative terms, the mean EF ranged between 0.38 and 0.77. Changes from the grass pixels largely dictated this variability (visually in Fig. 4 and Table 3). Average grass EF varied between 0.27 and 0.72. By contrast, the mean EF of trees only varied between 0.75 and 0.90. The variability in the grass layer is substantial, especially considering that all airborne flights, except 2015-07-03, were acquired during similar meteorological conditions (Table 1). By contrast, trees presented low inter and intra annual variability with mean EF maintaining consistent ranges throughout the different acquisitions. The mean tree EF interquartile range for all overpasses was 0.08 (Table 3). This pattern included those during the dry and hot summer (e.g. mean tree EF was 0.79 during midday of 2015-07-03). Within-scene variability was also greater for grass species compared to trees. The standard deviation of EF in the ROI ranged between 0.07 and 0.27 (mean 0.16) [LE: 40 and 84 W m^{-2}; mean 60 W m^{-2})] for the grass understory layer compared to 0.11 and 0.14 (mean 0.12) [LE: 27 and 53 W m^{-2}; mean 40 W m^{-2}] for the oak trees (Table 3). Interestingly, the summer acquisition of 2017-07-03 had the largest within-scene variability, for both vegetation canopies, with a standard deviation of 0.27 and 0.14 [LE: 141 W m^{-2} and 63 W m^{-2}] for grasses and trees, respectively (Table 3).

The model performance with the sharpened data at 1.5 m aligned very well with tower measurements (Fig. 5). Modeled H had 40 W m^{-2} RMSD and 15 W m^{-2} bias. Modeled LE demonstrated slightly more uncertainty with 57 W m^{-2} RMSD and − 3 W m^{-2} bias, due to the consistent Rn underestimation (bias: −33 W m^{2}), as LE is computed as the residual of the energy balance.

3.2. Spatial scale effects on modeled fluxes

3.2.1. Weighted average of parameters

The modeling performance using the airborne imagery at the different spatial scales showed that errors and biases tend to increase with coarser resolution data (Fig. 5). For images with 30 m resolution and greater, parameter values were weighted based on tree/grass cover (see Section 2.3.4). Crucially, the ability to discriminate between grass and tree pixels was a very important factor as demonstrated by the large increase in errors between the 10 m and 30 m spatial scales, i.e. H RMSD and bias increased from 67 and 50 to 95 and 78 W m^{-2}, respectively. Errors at 10 m resolution also increased compared to the more similar retrievals at 1.5 and 4.5 m.

As an example to visualize the different pixel sizes in relation to the tower footprint area, Fig. 6 shows the modeled LE at these different spatial scales for the airborne acquisition of 2016-05-03.

The LE histograms within the ROI (ignoring water and soil pixels) for 2016-05-03 are illustrated in Fig. 7. A bimodal distribution is clearly visible at 1.5 and 4.5 m with two peaks at around 450 and 600 W m^{-2} (Fig. 7a, b), stemming from the different distribution of tree and grass pixels. However, only one peak stands out at >4.5 m, with a clear

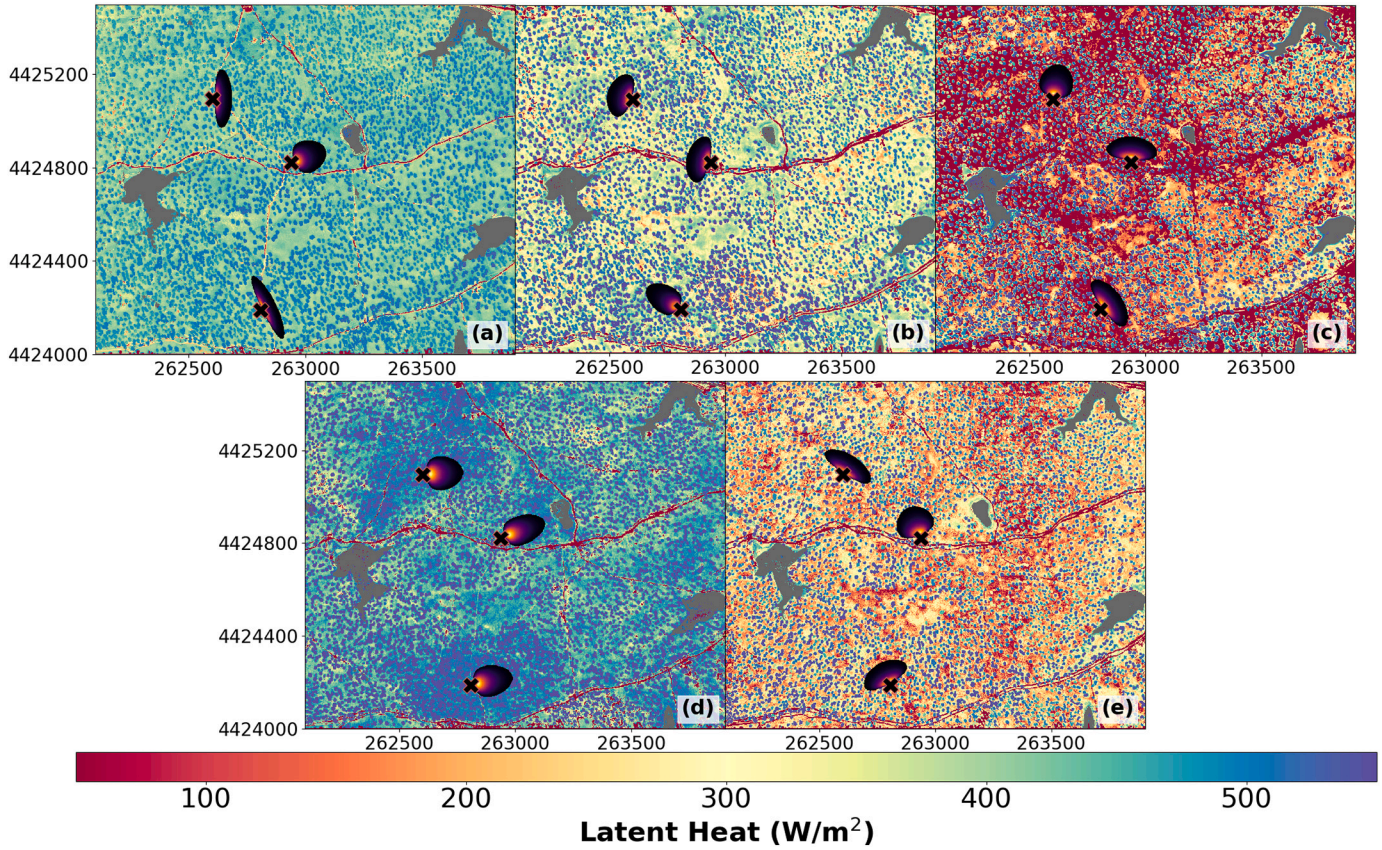

Fig. 4. Modeled TSEB LE (no data in grey) for the airborne overpasses with sharpened AHS LST and CASI imagery (1.5 m) for 2014-04-08 11:47 UTC (a), 2015-04-23 12:15 UTC (b) 2015-07-03 11:55 UTC (c) 2016-05-03 12:15 UTC (d) and 2017-05-19 12:17 UTC (e). Crosses represent the tower location and dark ellipses represent the respective tower footprint area of each tower during the overpass time step, where the yellow-purple points indicate a greater weighted contribution of the EC flux measurement (Kljun et al., 2015). The coordinates (on X-Y axis) are projected on UTM zone 30 N with units in meters. (For interpretation of the references to colour in this figure legend, the reader is referred to the web version of this article.)

Table 3
EF standard deviation (σ), first (Q1) and third (Q3) quartile (i.e. 25th and 75th percentile), and the interquartile range (Q3-Q1) within the ROI for the different airborne acquisitions at 1.5 m spatial resolution.

	2014-04-08			2015-04-23			2015-07-03			2016-05-03			2017-05-19			Average of all scenes		
	Grass	Tree	*Total*	Grass	Tree	*Total*	Grass	Tree	*Total*	Grass	Tree	*Total*	Grass	Tree	*Total*	Grass	Tree	*Total*
Mean (−)	0.72	0.81	*0.75*	0.58	0.79	*0.63*	0.27	0.79	*0.38*	0.72	0.90	*0.77*	0.40	0.75	*0.48*	0.54	0.81	*0.60*
Median (−)	0.72	0.83	*0.73*	0.59	0.82	*0.62*	0.31	0.82	*0.40*	0.75	0.92	*0.77*	0.41	0.78	*0.46*	0.56	0.83	*0.60*
σ (−)	0.07	0.11	*0.09*	0.14	0.13	*0.16*	0.27	0.14	*0.33*	0.14	0.11	*0.15*	0.16	0.13	*0.21*	0.16	0.12	*0.19*
Q1 (−)	0.70	0.80	*0.70*	0.53	0.77	*0.55*	0.19	0.77	*0.19*	0.71	0.89	*0.72*	0.32	0.73	*0.36*	0.45	0.79	*0.47*
Q3 (−)	0.75	0.85	*0.81*	0.65	0.85	*0.76*	0.58	0.87	*0.70*	0.78	0.94	*0.84*	0.50	0.82	*0.66*	0.63	0.87	*0.75*
Q3-Q1 (−)	0.05	0.05	*0.10*	0.12	0.08	*0.21*	0.39	0.10	*0.51*	0.07	0.05	*0.12*	0.17	0.10	*0.30*	0.18	0.08	*0.29*

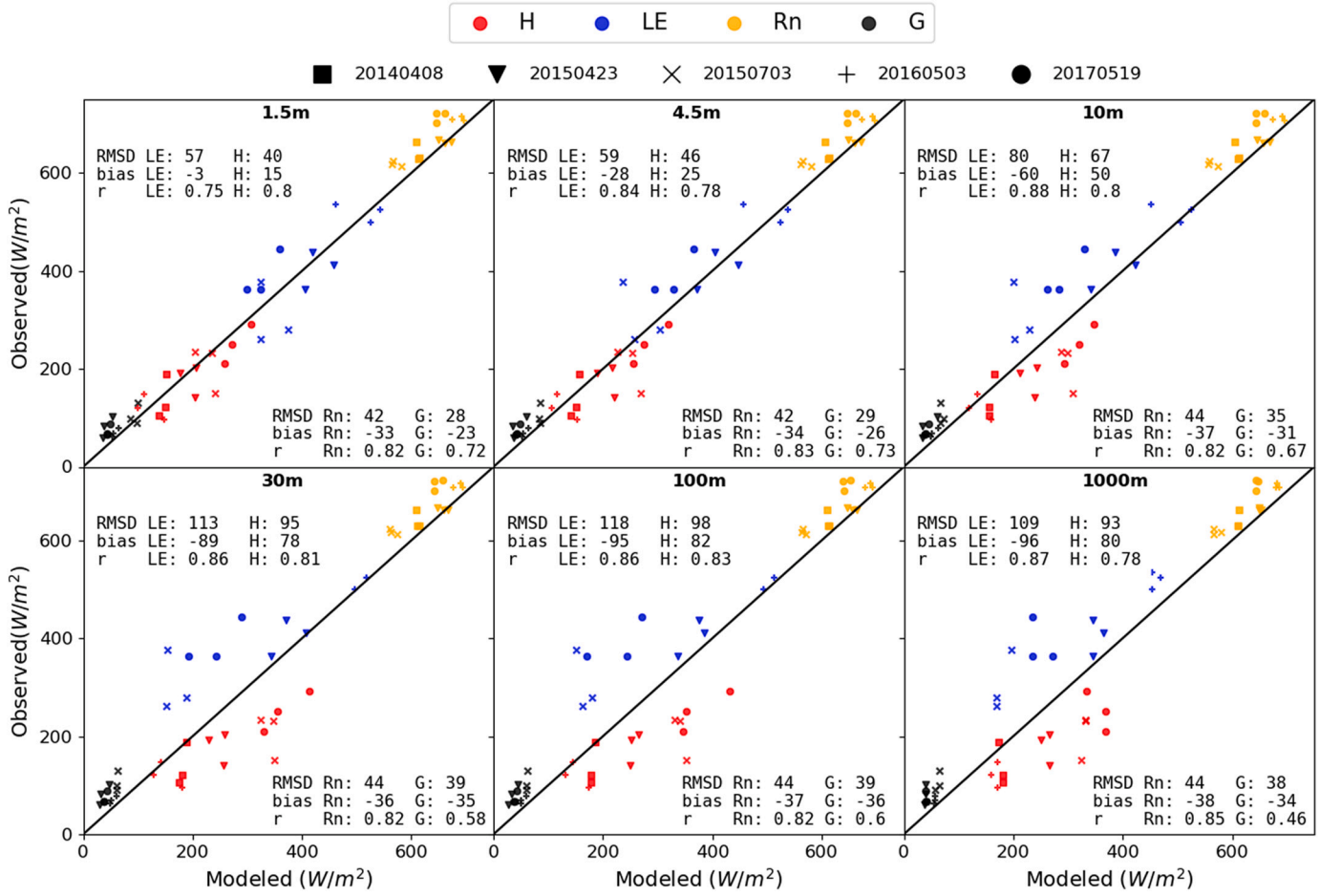

Fig. 5. Scatter plots of TSEB estimated fluxes H (red), LE (blue), Rn (yellow) and G (black) versus those measured from the EC towers (and black 1:1 line) for the retrievals with 1.5–1000 m spatial resolution when roughness parameters are estimated on a pixel basis based on its land cover type. Different symbols represent the different airborne acquisitions. (For interpretation of the references to colour in this figure legend, the reader is referred to the web version of this article.)

normalization effect. This was also the case for the 10 m simulations, even though tree and grass pixels had different parameterizations.

3.2.2. *TSEB-2S*

TSEB-2S is only applicable at coarser scales (Burchard-Levine et al., 2020), for simulations when the pixel size is unable to discriminate grass and tree features (i.e. ≥30 m). The TSEB-2S improved upon simply applying a weighted average to parameter values (Fig. 8 versus Fig. 5 for >10m). The H RMSD decreased from roughly ~100 W m^{-2} to ~55 W m^{-2}. H is still generally slightly overestimated (and, by consequence, LE underestimated) at all scales. The summer 2015-07-03 overpass, in which TSEB-2S was parameterized as a scattered tree-soil system, had the largest H overestimation notably at the 30 m and 100 m scale.

3.2.3. *Consistent effective roughness across scales*

When effective landscape roughness parameters (i.e. d0 and z_{0M}) are forced into TSEB and maintained consistent for all scales (from 1.5-1000 m), the retrieval errors for the model runs in Fig. 9 with mixed pixels (i.e. ≥30 m) decrease (RMSD of ~80 W m^{-2} for H) compared to the weighted average approach (RMSD of ~95 W m^{-2} for H; Fig. 5d, e, f). The forced z_{0M} of 0.6 m estimated through Raupach (1994) aligned relatively well against the estimated median z_{0M} (i.e. ~0.8 m) from the EC tower measurements (using Eq. (3.2) from Foken (2017) as proposed by Panofsky, 1984). This model approach assumes that mechanical turbulence occurs at a coarser scale than the size of individual elements (Hopwood, 1996; Mahrt, 2000; Mahrt, 1993; Vihma and Savijärvi, 1991). However, when discrimination of trees and grasses was possible at the pixel level (i.e. ≤10 m), errors increased (from ~50 to ~80 W m^{-2} for H) compared

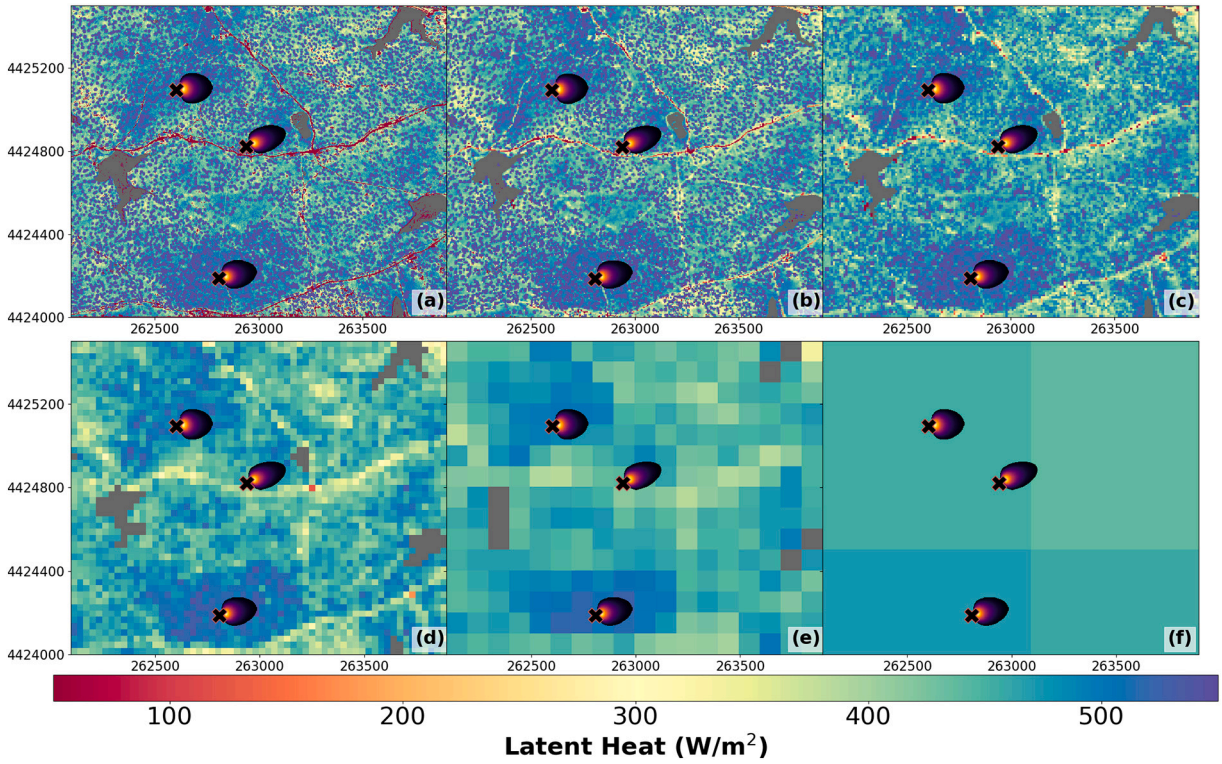

Fig. 6. Modeled TSEB LE for 2016-05-03 12:15 UTC at 1.5 m (a), 4.5 m (b), 10 m (c), 30 m (d), 100 m (e) and 1000 m (f). Crosses and black ellipses represent the tower location and their respective footprints, where the yellow-purple points indicate a greater weighted contribution of the EC flux measurement (Kljun et al., 2015). The coordinates (on X-Y axis) are projected on UTM zone 30 N with units in meters. (For interpretation of the references to colour in this figure legend, the reader is referred to the web version of this article.)

to when roughness parameters were estimated separately for tree and grass pixels (Fig. 5a, b, c). Errors maintain relatively constant bounds for all the spatial scales assessed (1.5−1000 m), with RMSD of H ranging between 74 and 85 W m^{-2} for H.

3.3. Sen-ET product

Compared against the three EC tower measurements, the 20 m (Sen-ET$_{20m}$) and 1 km (Sen-ET$_{1km}$) Sen-ET products largely underestimated H with a bias of −72 and − 85 W m^{-2}, respectively. Both products achieved similar performance and patterns. Sen-ET$_{20m}$ underestimated H slightly less. Rn was also underestimated while G was overestimated, causing for a large underestimation in AE. However, since H was also significantly underestimated, the LE residual had fewer errors compared to the measured fluxes at the tower (RMSD of 73 and 84 W m^{-2} for Sen-ET$_{20m}$ and Sen-ET$_{1km}$, respectively).

Roughness parameterization was very similar at both spatial scales. Sen-ET assigns vegetation structural parameters based on the CCI LCC map. As the map indicated that the ROI was 'Herbaceous cover' or 'Mosaic cropland', the h_c assigned was much lower compared to what is observed in the field. The h_c used in Sen-ET lies roughly between 0.1 and 0.15 m and the f_c parameter was set to 0.5 or 1. Both of these parameter values are closer to "grass-soil" rather than "tree-soil" parameterization from Table 2, even though a greater number of observations occur during the summer season due to less frequent cloudy conditions.

The AHS airborne acquisition from 2017-05-19, resampled to 30 m (AHS$_{30m}$), was compared to the Sen-ET(−like) product (Sen-ET$_{30m}$) of the same date, as described in Section 2.4. The retrieved EF was relatively similar in magnitude (bias: −0.04 and RMSD: 0.09) for both products even though the pixel-wise correlation was low (r = 0.31) (Fig. 11).

When comparing the sharpened Sentinel-3 and the aggregated 30 m LST on 2017-05-19 (Fig. 12) the correlation between the vegetated pixels (ignoring water pixels) was relatively low (r ~ 0.5) with an RMSD of ~2 K (using the AHS LST as the reference). The dynamic range in values was much lower for the sharpened Sentinel-3 LST compared to AHS LST.

4. Discussion

LE and H estimates with TSEB were most accurate when the pixel size was small enough to discriminate between the tree and grass signals. The simulations of LE and H at 1.5 m had consistently the least errors when compared against the EC data. Results were similar with the 4.5 m pixel size, but RMSD and bias of H slightly increased from 40 and 15 W m^{-2} to 46 and 25 W m^{-2}, respectively. The thermal sharpening method to achieve an LST of 1.5 m improved the separation of these pixels. This reduced the flux retrieval errors through a more adequate parameterization compared to using the original data at 4.5 m. However, both are still within range of the typical uncertainty of daytime EC measurements of H and LE (~50 W m^{-2}; Kustas and Norman, 2000, 1997). Even though discrimination between trees and grass pixels was still possible at the 4.5 m pixel size, edge effects between pixels from the two vegetation layers, and/or other land covers such as water and soil, were slightly more pronounced. Mixed pixels classified as trees had thermally higher temperatures due to the adjacent grass signals. This effect was more pronounced and notable when the temperature of trees and grasses were very different, such as during the summer acquisitions. This, combined with roughness values indicating a surface better aerodynamically coupled with the atmosphere (i.e. scattered tree landscape), caused for lower resistance values that resulted in an overestimation of H, leaving less AE for LE (sometimes no available energy for LE, i.e. LE = 0 W m^{-2}). Assigning the mean values of the center-most pixels to the entire tree crown minimized these situations. However, these edge effects still occurred, especially for trees with smaller crowns. The tree boundary effects were even more important at the 10 m pixel size and resulted in

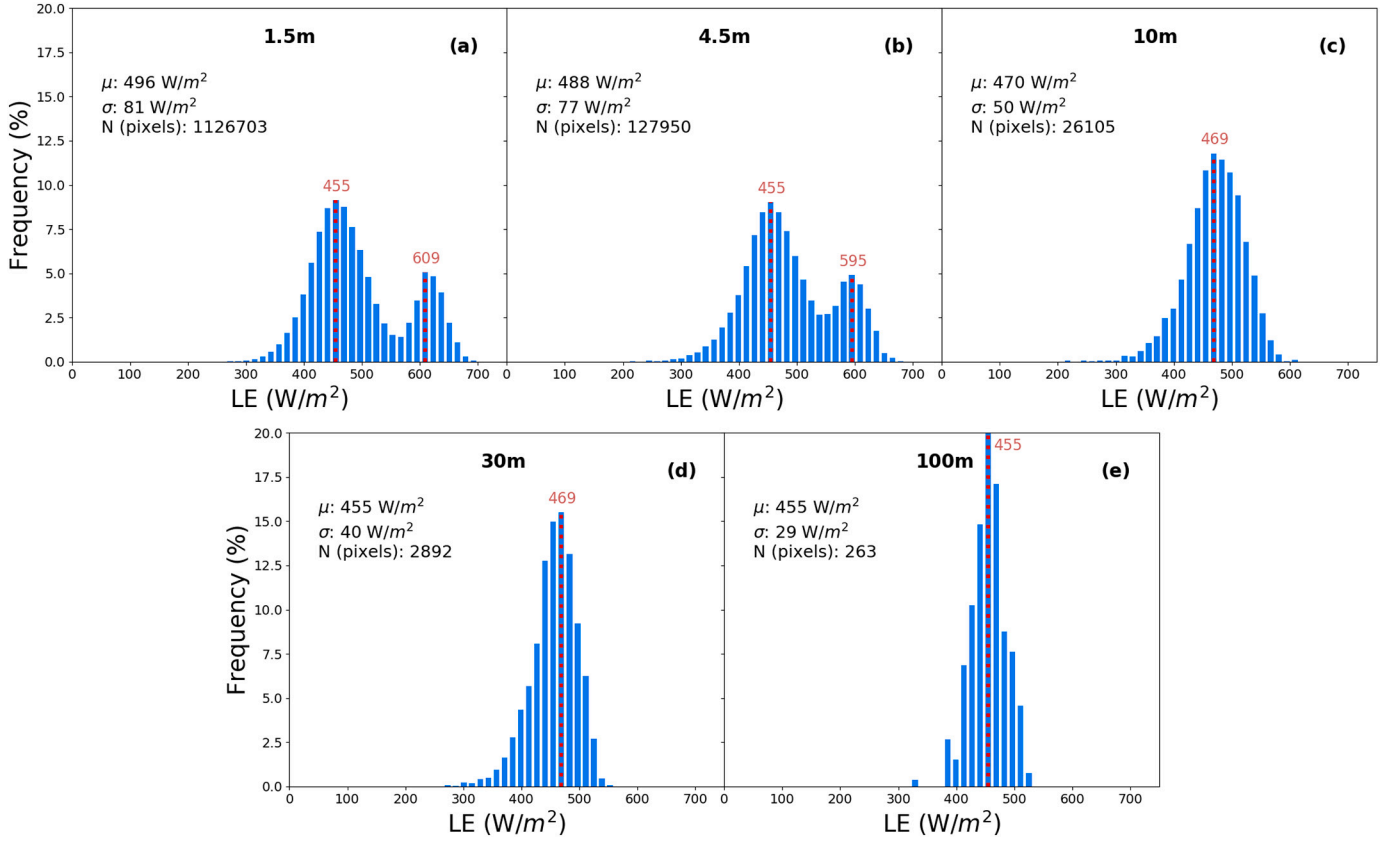

Fig. 7. Histograms of estimated LE distribution within ROI for acquisition on 2016-05-03 for simulations at 1.5 m (a), 4.5 m (b), 10 m (c) 30 m (d) and 100 m (e) spatial resolutions.

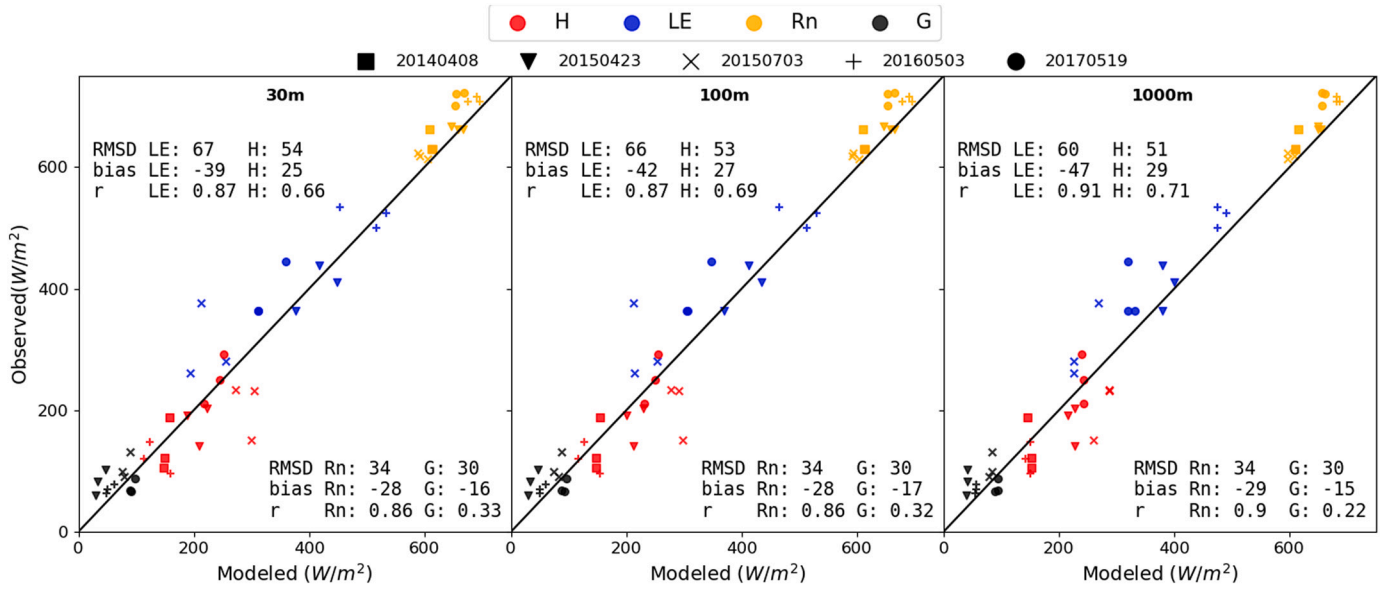

Fig. 8. Scatter plots of TSEB-2S estimated H, LE, Rn and G fluxes versus those measured from the EC towers (and black 1:1 line) for the retrievals with 30, 100 and 1000 m spatial resolutions when roughness parameters are estimated on a pixel basis based on seasonality (TSEB-2S).

larger errors compared to the 1.5 and 4.5 m simulation runs. At 10 m, the imagery can just about discriminate tree pixels for larger tree crowns, with mean tree diameter within the study site being roughly ~8.2 m (Pacheco-Labrador et al., 2017). Therefore, trees were depicted by one or two pixels, but are much more thermally mixed with grass (and/or other) signals. This issue was particularly notable during the summer acquisitions (i.e. 2015-07-03 and 2017-05-19), when the difference between the grass and tree LST was very large. As shown in Fig. A3, the number of tree pixels with insignificant LE (i.e. LE = 0 W m^{-2}) per total number of tree pixels in the ROI tended to increase with pixel size, notably for the summer acquisitions.

The average of the inputs (i.e. LST, LAI and f_g) within each of the

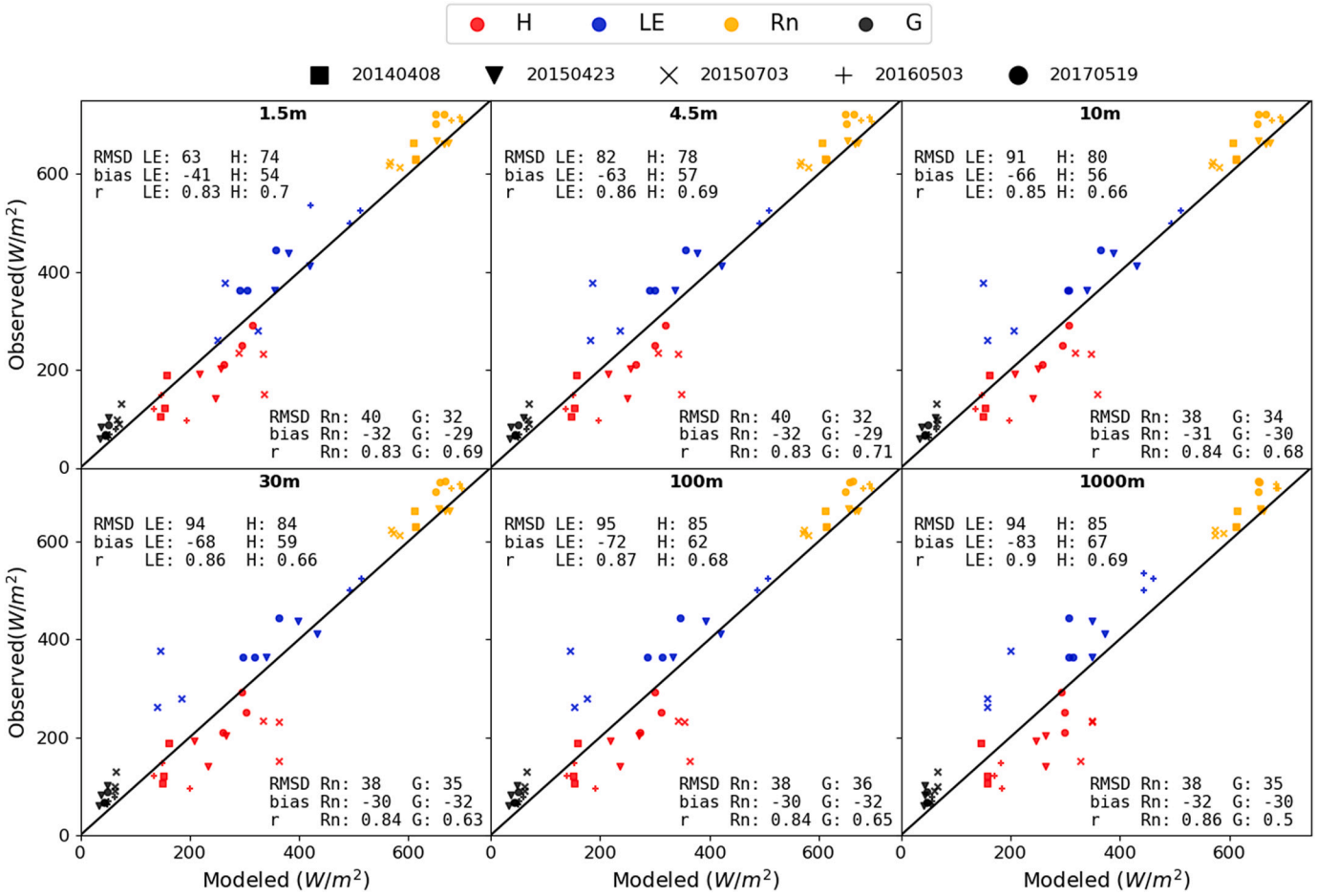

Fig. 9. Scatter plots of TSEB estimated H, LE, Rn, G fluxes using constant effective roughness (i.e. d0 and z0M) values for all scales versus those measured from the EC towers for the retrievals with 1.5–1000 m spatial resolutions.

tower footprints do not significantly change at the different spatial scales (Table A1). This suggests that greater errors are due to the modeling structure and parameter values. When pixel mixing increases with larger grid sizes, the modeling structure does not adequately depict the dual vegetation layer using a single vegetation source representation. This issue happens even when adjusting parameters as a weighted average of the two vegetation covers. This demonstrates the non-linear relationship between model inputs and flux estimates as discussed for other heterogenous landscapes such as in Kustas et al. (2004), Kustas and Norman (2000) and Moran et al. (1997). These studies showed that pixel averaging techniques for these input variables lead to important errors in modeled energy fluxes within sites of varying land cover. As discussed in Moran et al. (1997), errors in H retrievals were associated to sites with patchy vegetation and subpixel variability in cover and roughness. In this study, the aerodynamic resistance terms (Ra and Rs) decreased at the coarser simulations ($\geq$ 30 m; Table A1). This resulted in the increase of the estimated component temperatures (T_s and T_c), which by association increased the modeled aerodynamic temperature T_{AC} (Table A1), resulting in the H overestimation, and subsequent LE underestimation, at these resolutions (Fig. 5). Ershadi et al. (2013) also pointed to this problem. In their study with the SEBS (Su, 2002) model, aerodynamic resistance (i.e. Ra) decreased with coarser data (ranging from 240 m to 960 m pixel sizes), leading to greater errors in estimated H. Similarly, using UAV acquisitions over a clumped vineyard and TSEB with dual temperatures measurements (TSEB2T; Nieto et al., 2019), Nassar et al. (2020) observed increases in H at larger grid sizes, from 3.6 to 30 m, due to the decrease in aerodynamic resistance. In our study, all flux retrievals at 30 m or greater pixel size resulted in very similar error statistics due to comparable levels of pixel heterogeneity at these scales. Within the ROI, inter-pixel signal variability is not very large at these coarser scales, as the tree canopy cover and density remain relatively consistent over the herbaceous layer. This, thus, makes the study site seem relatively homogenous at larger scales as it pertains to a single land cover classification (e.g. TGE or Savanna). However, these results indicate that the small-scale structural differences of the two vegetation elements were large enough to have an important impact on modeled turbulent heat fluxes, and these differences should be dealt with in order to obtain reliable results with land surface modeling methods.

The adequate representation of roughness (i.e. d0 and z_{0M}) for mixed pixels at coarser scales ($\geq$30 m), along with their non-linear relation with the flux output, was the main driver for the increased errors compared to the finer resolution (<10 m) model runs. This was further supported when roughness parameters were forced into TSEB and maintained constant for the different grid sizes using an effective roughness value (Section 3.2.3). The error statistics remained relatively stable throughout the aggregations and improved upon the weighted average approach. Since the distribution of the main roughness elements (i.e. trees) remain relatively consistent throughout the ROI, the use of a constant effective roughness lengths across scales was a sound approach to depict surface roughness. As Hopwood (1996) demonstrated, the near-surface turbulence of a heterogeneous surface at a certain vertical height is approximately homogeneous across different spatial scales, with the effective roughness length of momentum fluctuating little for increasingly larger scales (Hopwood, 1996).

The TSEB-2S approach also improved the modeling performance for coarser resolution model runs (RMSE of H: ~55 W m^{-2}). As discussed in

Burchard-Levine et al. (2020), the assumption of a dominant vegetation layer for different phenological periods improved the turbulent flux exchange depiction for a three-source ecosystem (tree-grass-soil) with large seasonal changes using a two source modeling representation (vegetation-soil). TSEB-2S separates the modeling period between the two major situations occurring in these ecosystems: 1) tree, grass and soil all contribute to ecosystem fluxes and 2) grass is not photosynthetically active and only tree and soil contribute to total fluxes. As such, different modeling parameterizations were applied according to the assumed dominant vegetation structure, better representing the surface characteristics. During the grass growing period, both tree and grass species are active but, since ~80% of the surface is covered by grass understory (with the other 20% being mostly tree canopies), TSEB-2S assumes that the grass-soil substrate dominates during these periods and neglects the heat and water flux contribution of the trees, but they still contribute to momentum through increased roughness as compared to a single homogeneous grass canopy. Perez-Priego et al. (2017) also supports this, showing that the understory layer dominates LE in this site. These simplifications cause for uncertainty, notably during seasonal transition periods when grass and trees co-dominate. However, these periods tend to only last a few weeks (Burchard-Levine et al., 2020). The TSEB-2S model configuration improved the modeling performance within these complex landscapes while maintaining the dual-source model structure, but it still had larger errors compared to the high resolution runs when grass and tree pixels were parameterized separately. The summer acquisitions, especially 2015-07-03, had slightly larger H overestimations compared to when TSEB-2S considers grassland to be the dominant vegetation structure during the growing season. This may be partly due to some grass species still being active while the tree-soil representation ignores grass transpiration in TSEB-2S. In addition, the roughness of the 'soil' source (which is composed of dry grass) during the summer may not be well depicted even though the b coefficient for the Rs computation (Eq. (8)) was increased to partly account for this (Burchard-Levine et al., 2020; Kustas et al., 2016). It should be noted that relatively few data points were used in this study and possible 'outliers' have more impact on error statistics. For instance, the NPT tower on 2015-07-03 12:00 had an H measurement of ~150 W m^{-2} while the two other towers (CT and NT) measured roughly 250–280 W m^{-2} at the same time step. The modeled H is largely overestimated at this data point at all scales and approaches used within this study.

Rn was consistently underestimated (bias: ~ − 35 W m^2) for all model runs. This largely stemmed from the overestimation of outgoing LW radiation (data not shown) and, slight overestimation of surface effective albedo (data not shown). Therefore, this issue led to the underestimation of both net LW and SW radiation. Tree shadows over the understory may influence these results since these were not considered in this study (nor within TSEB). Shadows would decrease the albedo and temperature, and thus, decrease both SW and LW outgoing radiation. Analysis of the CASI imagery indicated that shadows represented only 4–6% of the ROI, but may still partly influence the slight, but consistent, underestimation of modeled Rn. TSEB-2S had slightly less bias in Rn (bias: ~ − 28 W m^2), which was almost entirely due to improvements during the summer acquisitions, particularly for 2015-07-03. The decrease in the assumed f_c in TSEB-2S (i.e. f_c= 0.2 for summer period) led to a decrease in modeled albedo and surface emissivity, due to the greater weight for the soil source. Subsequently, this decreased outgoing LW (decrease in emissivity) and SW (decrease in albedo) radiation, leading to less Rn underestimation. Guzinski et al. (2020) evaluated ET retrievals with Sentinel-2 and Sentinel-3 data for different sites. They also found large underestimations of Rn for sites with savanna land cover types. These authors attributed this to the vegetation being more sparse causing for greater uncertainties in the estimation of albedo and emissivity (Guzinski et al., 2020). Additionally, the relatively simple radiation transfer scheme within the TSEB may not adequately simulate the complex structural features of the tree canopies, which, for example, may induce multiple scattering of radiation within the canopy. More advanced and 3D radiative transfer modeling, such as the Discrete Anisotropic Radiative Transfer (DART) model (Gastellu-Etchegorry et al., 2015), could better incorporate and characterize the angular and shadow effects on LST and albedo (e.g. such as in Guillevic et al., 2013), and its effect on modeled heat and water fluxes. Errors in Rn directly translate into errors of LE, since LE is computed as the residual of the energy balance. Because of this, LE tended to have larger errors compared to H but still within accurate ranges (RMSE ~60 W/m^2 for high resolution runs) since the Rn errors were not substantially large (RMSE ~40 W/m^2).

When evaluating remote sensing products with tower-based measurements, the mismatch between pixel size and EC footprint area is another source of uncertainty. However, the ROI is relatively homogeneous at larger scales. Water and soil pixels only account for ~4% of the ROI, with the rest being vegetated tree and grass pixels, according to the CASI LCC of all overpasses. The distribution of water bodies might also affect the micrometeorological conditions, but they are only captured at the 1000 m spatial grid scale. Despite this, the water bodies lie outside the flux tower footprints for all scenario assessed in this study. Therefore, this problem was not a significant issue in this study. In fact, Pacheco-Labrador et al. (2017) reported for the same case study that the spatial mismatch between EC and remote sensing footprints was not an important contributor to errors in remote sensing-based gross primary production (GPP) estimations. In addition, since the within pixel heterogeneity remains relatively constant across these scales, the coarse model runs at 30, 100 and 1000 m had also very similar error statistics. Only at 1000 m, conditions that are not entirely captured in the footprint area may influence the pixel value. The pixels are much more aligned to the footprint area at finer resolutions (≤100 m). The largest difference occurred for the NPT tower at the 1000 m spatial run for the overpass in 2015-07-03, where LE decreased substantially and the errors decreased compared to the runs from 30 and 100 m. Only 4 pixels represent the ROI at 1000 m, where the CT and NT are both located within the same pixel while the NPT tower lies in a different, more southern, pixel. For the NPT tower on 2015-07-03, the mean LST over the 'footprint' decreased by ~2.5 K compared to the LST at 1.5 m. This is by far the most significant change in LST for any of the overpasses and tower footprints. The greater density of trees towards the west of the tower, not measured by the tower footprint, but captured at the 1000 m grid may explain this. While the NPT footprint composition is similar to both CT and NPT (El-Madany et al., 2018), the greater surrounding area of NPT has a larger density of trees, which influences the surface temperature. In fact, the 1000 m pixel of the NPT tower had a tree fractional cover of about ~29%, larger compared to the 22% observed over its footprint and larger compared to the 1000 m pixel associated to both CT and NT towers (23%). The effects are more significant during the summer months when the difference between tree and grass pixels are very large and, thus, will have a larger impact on LST and modeled fluxes. The grass already began to senesce on the 2017-05-19 overpass, also demonstrating a decrease of LST (~1.5 K) for NPT at the 1000 m scale. The rest of the overpasses did not observe such changes to LST, and hence in the model performance. As such, the most important changes due to the spatial mismatch between tower footprint and pixel size occur at 1000 m for the NPT tower. These changes were accentuated during the summer months when the different density of trees has a larger impact on LST compared to when the grass understory is more active.

The high-resolution simulations at 1.5 m demonstrated important spatio-temporal variability within the ROI, notably for the grass species. The growing season is largely limited by water availability and strongly correlated with precipitation (Luo et al., 2018). This causes for important inter-annual variability of LE, typical in semi-arid TGE (Allard et al., 2008; El-Madany et al., 2020; Luo et al., 2018; Ma et al., 2007). This may explain the important differences in the average EF observed during similar seasonal periods for the different years studied. By contrast, trees presented low inter and intra annual variability with mean tree EF maintaining consistent ranges throughout the different acquisitions,

including those during the dry and hot summer period. As trees have larger root systems to access water deeper within the soil allowing for relatively constant functioning, these different responses were very much in line with previous works studying ecosystem dynamics in Mediterranean TGE (e.g. Luo et al., 2018). In addition, the stable LAI used for trees may also contribute to the low variability observed. By contrast, the grass understory is very diverse with a variety of species co-existing at different phenological stages within the same seasonal period. As such, micro-climatic processes (e.g. tree shadows, micro topography) may induce a certain degree of variability even within a relatively small ROI of a seemingly homogeneous herbaceous understory. The largest within scene variability was observed during the summer acquisitions, particularly for 2015-07-03. The effect of isolated trees over the grass layer was likely more pronounced during the hot and arid summer conditions, causing for this increased variability. As shown and discussed in Moreno and Pulido (2008) in a similar TGE, temperature was significantly lower beneath the trees on warm days, and soil water content tended to be higher closer to the trees. Destructive biophysical grass measurements (e.g. LAI and canopy water content) were sampled during the overpass dates described in this study, with certain plots located beneath the influence of the tree canopy and others in open grassland. However, these two sets of measurements rendered no significant differences (data not shown), suggesting that the surface temperature and soil moisture drove the variability.

The Sen-ET product simulated LE with similar accuracy as the LE retrievals with airborne imagery when roughness parameters was forced into TSEB (Fig. 10). Both scales achieved similar error statistics, though the sharpened product (20 m) slightly improved model performance. This may be linked to a greater mismatch between pixel size and tower footprint at the original resolution of ~1 km, as discussed above. However, the relatively good LE retrievals from Sen-ET were compensated from large errors in the other flux components cancelling each other, since LE is computed as a residual. H was significantly underestimated (RMSD ~100 W m^{-2}) as well as the AE. The increase in modeled resistance due to the much lower h_c estimated by Sen-ET largely explained the substantial H underestimation in Sen-ET due to the land cover misclassification from the CCI map. This is a similar, but inverted, situation to the lower resolution (≥30 m) runs with weighted average of parameters (Fig. 5), where H was significantly overestimated (RSMD ~100 W m^{-2}) due to underestimation of model resistances. Guzinski et al. (2018) employed a methodology very similar to Sen-ET, except for the landcover parameterization, which was based on Corine rather than the CCI land cover maps. In that study, the Majadas ROI was classified as agro-forestry and assigned an h_c of 8 m and an f_c varying with spectral reflectance, resulting in RMSD of around 50 W m^{-2} at both spatial scales. These results demonstrate the issues and uncertainties of global flux products over TGEs, which often have greater uncertainty for land cover mapping (e.g. Giri et al., 2005). This further exacerbates the uncertainty of assigning singular and aggregated parameter/input values into mixed pixels with numerous roughness elements, as illustrated from this study and supported by previous works (Kustas et al., 2004; Mahrt, 1993; Moran et al., 1997; Vihma and Savijärvi, 1991). Other regional ET products tested also had large errors (e.g. LSA-SAF ET; see Fig. A4).

The local airborne acquisition from 2017-05-19 was spatially compared to a Sen-ET(−like) product from the same date. The magnitude of the output EF from both datasets do not change drastically even though the correlation was low ($r = 0.31$). The sharpened Sentinel-3 (30 m) LST, used as an input, had a much lower range in values compared to the observed ASH LST (resampled to 30 m). Table A2 shows the mean and range of LST values within the three EC tower footprints. As shown, the mean LST within the footprint was similar, especially considering that the Sentinel-3 overpass time of ~10:25UTC occurs about 40mins prior to the AHS overpass of 11:08 UTC. However, the range in values was much higher for the AHS sensor in all three footprints. These suggest that the LST sharpening procedure did not effectively capture the entire variability present in high-resolution observations. The original coarse resolution (i.e. ~1 km) has aggregating effects where the more extreme values are not present in the original observations as already discussed in Bellvert et al. (2020). In fact, these differences in LST from the two products explained a large portion of the variability of the difference in EF output ($r = -0.69$; Fig. A5). However, while there were important differences in both LST datasets, and these differences were related to the changes in EF, the magnitude of the flux outputs do not differ drastically (Fig. 11). As such, according to these results, the sharpening method (i.e. DMS) seems to be a viable approach to obtain higher resolution (i.e. field scale) LST for ET modeling, even though the sharpening did not capture the entire LST dynamic range and hence moderate errors were present. This type of methodology allows to fill the current gap in the availability of a satellite based TIR sensors with a high temporal and spatial resolution (Guzinski et al., 2020; Guzinski and Nieto, 2019). However, the sharpened Sen-ET_{20m} product did not significantly improve model results in this study site (Fig. 10) as similar levels of within pixel heterogeneity are present at both scales for this landscape. It should be noted that the TIR sharpening procedure should be more effective with the Sentinel-2 MSI (compared to the Landsat-8 OLI) since it has greater spectral (i.e. 3 additional bands in the red-edge) resolution (Guzinski and Nieto, 2019). As well, the sharpened LST could yield more accurate results in landscapes where the main roughness elements change at scales that are captured with 20 m resolution (e.g. cropland

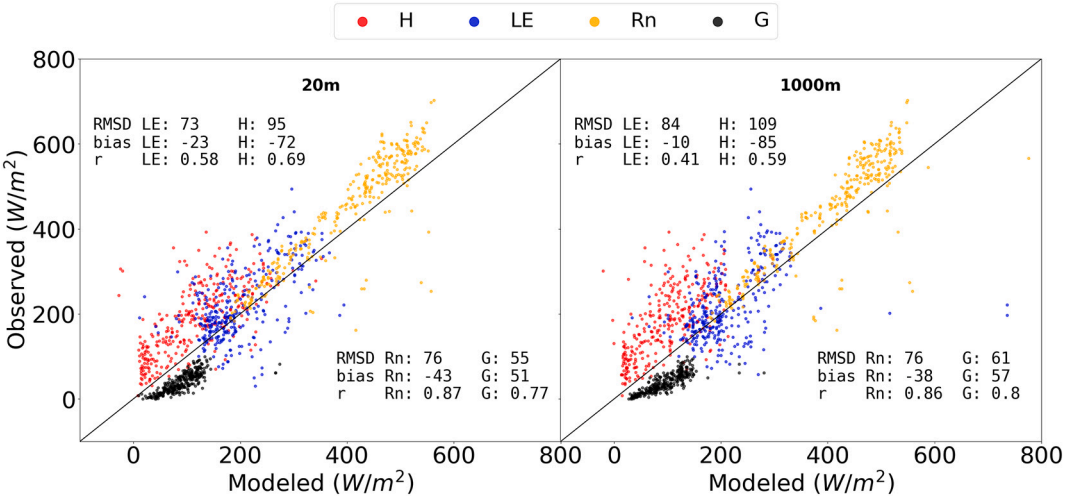

Fig. 10. Scatter plots of estimated H, LE, Rn, G fluxes for the 20 and 1000 m Sen-ET products versus those measured from the EC towers.

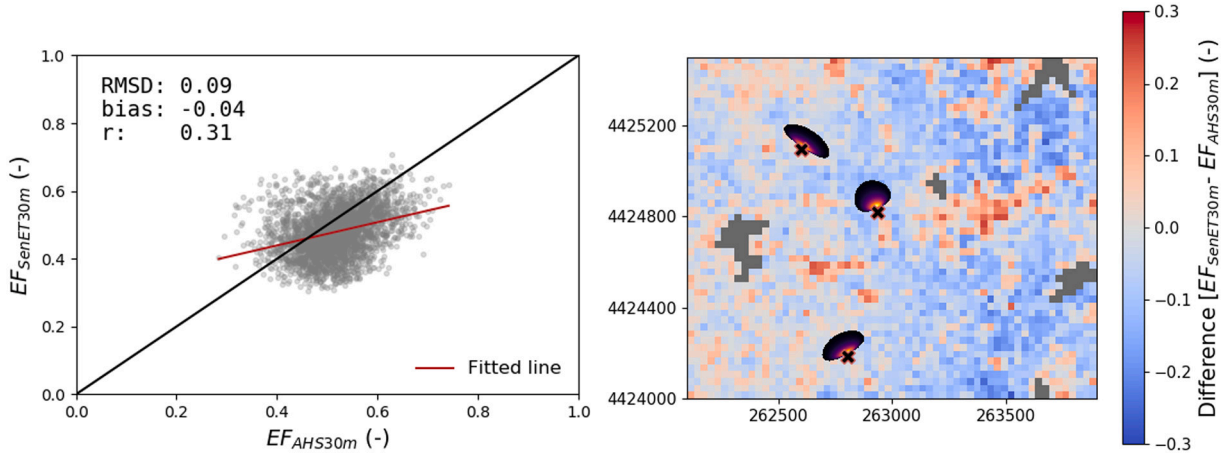

Fig. 11. Scatter plot of Sen-ET_{30m} EF versus AHS_{30m} EF on 2017-05-19 (left) and the difference map of Sen-ET_{30m} EF minus AHS_{30m} EF (30 m) (right). Water pixels masked in grey.

mosaics). This way, it would complement the sufficiently detailed roughness characterization within the TSEB model.

5. Conclusions

Findings from this study demonstrated that TSEB can accurately simulate ET (and related energy fluxes) in a heterogeneous TGE using remote sensing data when the pixel scale was sufficient to discriminate between the multiple vegetation structures present (i.e. trees and grasslands). The high-resolution airborne (1.5 m) demonstrated different spatial and temporal patterns between trees and grasses. Within a relatively small ROI (~1.5 km × 1.5 km), large variability in LE retrievals were observed for grasses. Trees also showed within scene LE variability, although less significantly than grasses. Nevertheless, they maintained similar flux averages throughout all the overpasses, including those acquired during the summer drought. The DMS thermal sharpening method (Gao et al., 2012) improved flux retrievals in this landscape by better separating the tree and grass thermal signals at 1.5 m compared to the original 4.5 TIR data. However, model uncertainty drastically increased at coarser spatial resolution (i.e. 30, 100 and 1000 m) when the pixels are mixed. Model performance remained relatively constant between the pixel sizes of 30 to 1000 m, with within pixel heterogeneity being similar at all these scales. The increases in errors were largely driven by the within pixel heterogeneity (i.e. mix of tree and grass) in larger grid sizes that did not adequately depict the landscape roughness and aerodynamic resistance. The TSEB model performance at coarser resolutions (i.e. ≥30 m) improved by forcing constant landscape roughness values for all spatial scales or, particularly, by applying TSEB-2S, where different parameterizations were used depending on the phenological period.

The larger uncertainties in coarser model runs were also confirmed by evaluating the Sen-ET satellite product over the study area for the entire year of 2017. The Sen-ET products showed similar errors statistics for both sharpened (20 m) and coarse (1 km) flux products and were comparable to the ranges obtained by the coarser (i.e. >10 m) airborne simulations. These results suggest that care should be taken when using global ET products over TGE and similarly heterogenous landscapes with multiple vegetation layers. Even though these ecosystems are apparently homogeneous at coarser resolutions, the presence of vastly different vegetation structures causes for heterogeneity at the pixel level when the spatial resolution is greater than 10 m. This issue induces large uncertainties in the modeling performance, if not accounted for. Results demonstrated that the different structural and physical characteristics of the isolated trees and grassland understory have a large impact in the energy balance of TGEs. These differences should be inherently incorporated within the modeling procedure to obtain robust turbulent flux estimates with remote sensing based SEB approaches.

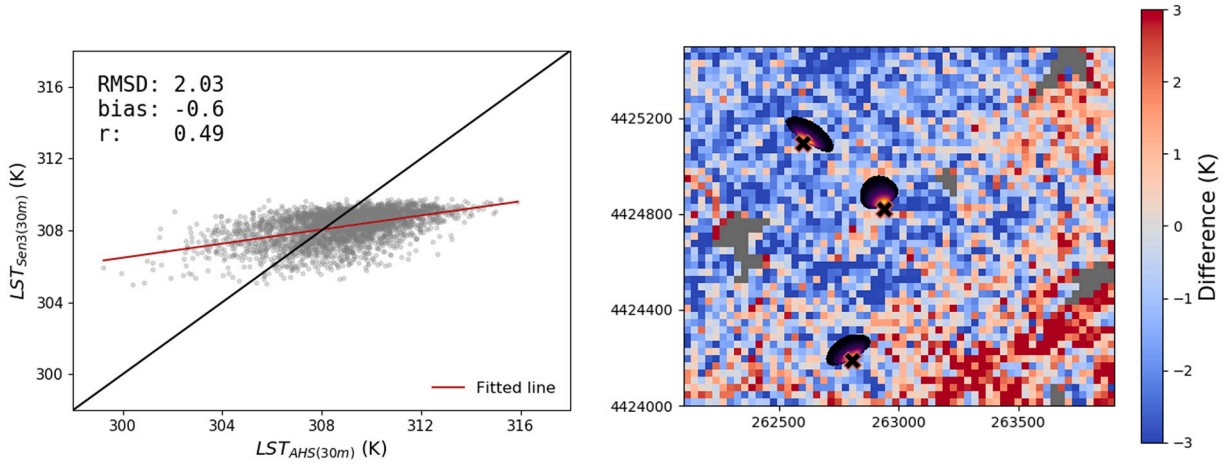

Fig. 12. Scatter plot of Sentinel-3 sharpened LST (30 m) [~10:25 UTC] and AHS aggregated LST (30 m) [11:08 UTC] (left) and the difference map of Sentinel-3 sharpened LST (30 m) minus AHS aggregated LST (30 m) (right). Water pixels masked in grey.

Author contributions

All authors contributed to discussing and improving the manuscript. MPM, HN, DR and VBL designed and formulated the research. MM and AC designed the experimental infrastructure. VBL analysed the data, created the figures, and wrote the manuscript. AC, MM, TSEM collected eddy covariance and biomet data. RG provided the Sen-ET dataset. MPM sampled and analysed in-situ grass LAI and spectral measurements.

Funding

The research received funding from the European Union's Horizon 2020 research and innovation programme under the Marie Sklodowska-Curie TRuStEE project (grant agreement No 721995). It was also funded by Ministerio de Economía y Competitividad through FLUXPEC CGL2012-34383 and SynerTGE CGL2015-G9095-R (MINECO/FEDER, UE) projects. The research infrastructure at the measurement site in Majadas de Tiétar was partly funded through the Alexander von Humboldt Foundation, ELEMENTAL (CGL 2017-83538-C3-3-R, MINECO-FEDER) and IMAGINA (PROMETEU 2019; Generalitat Valenciana).

Credit author statement

All authors contributed to discussing and improving the manuscript. MPM, HN, DR and VBL designed and formulated the research. MM and AC designed the experimental infrastructure. VBL analysed the data, created the figures, and wrote the manuscript. AC, MM, TSEM collected eddy covariance and biomet data. RG provided the Sen-ET dataset. MPM sampled and analysed in-situ grass LAI and spectral measurements.

Declaration of Competing Interest

The authors declare that they have no known competing financial interests or personal relationships that could have appeared to influence the work reported in this paper.

Appendix A

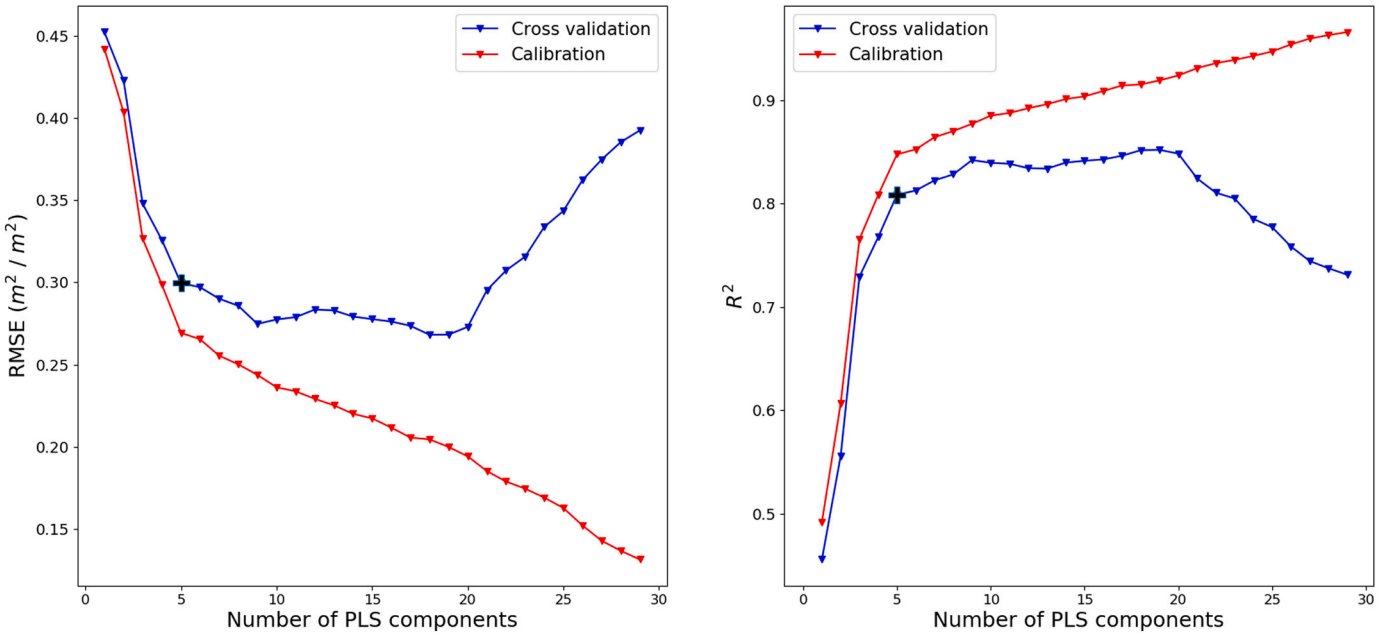

Fig. A1. RMSE (left) and R^2 (right) of the Partial least square regression (PLSR) model for predicting LAI with increasing PLS components for calibration (red) and 10-fold cross-validation (blue). (For interpretation of the references to colour in this figure legend, the reader is referred to the web version of this article.)

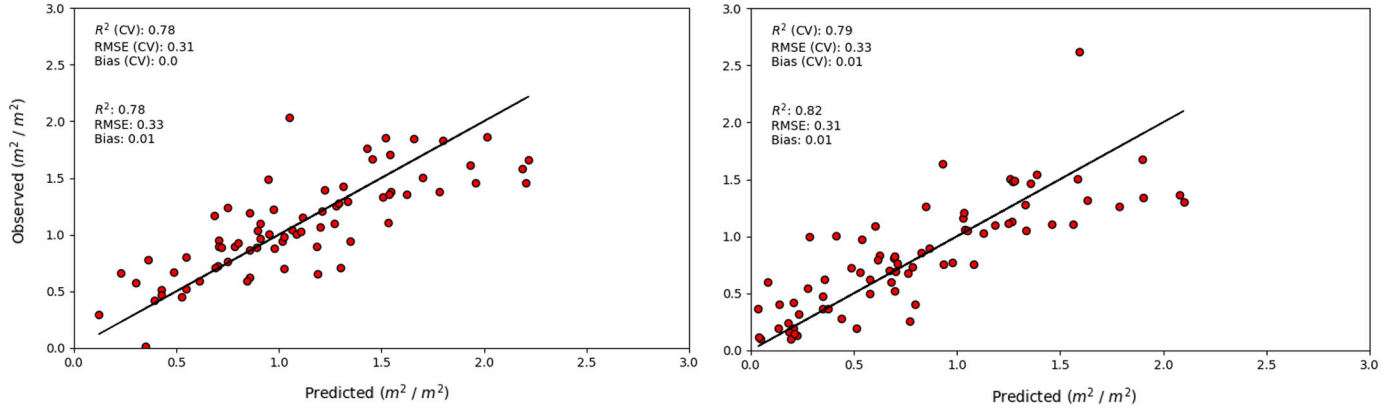

Fig. A2. Partial least square regression (PLSR) model (five components) to predict LAI (left) and LAIg (right) applied on the validation dataset from ground measurements of ASD spectral data (resampled to mimic the 136 CASI bands between 400 and 1005 nm) and destructive LAI measurements.

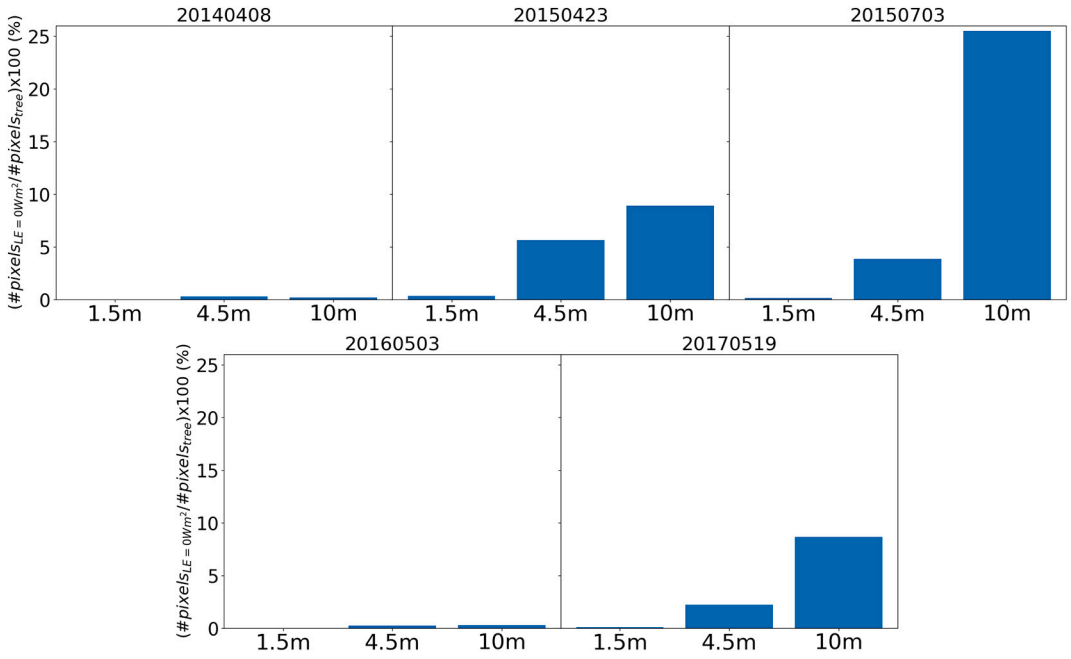

Fig. A3. The number of tree pixels where simulated Latent heat flux (LE) equals 0 (W m^{-2}) divided by the total number of tree pixels within the ROI (in %) for simulations when tree and grass pixels were distinguishable (i.e. 1.5 m, 4.5 m and 10 m).

Table A1
The average change of TSEB inputs and variables at all three tower footprints for all airborne overpasses with respect to the simulation at 1.5 m spatial resolution.

	4.5 m	10 m	30 m	100 m	1000 m
LST (K)	+0.024	−0.022	−0.068	−0.061	+0.053
LAI (m^2 m^{-2})	−0.001	+0.002	+0.011	+0.032	−0.066
f_g (−)	***−0.001***	***+0.001***	***+0.005***	***+0.002***	***−0.020***
Ra (s m^{-1})	+0.620	+1.894	−9.518	−9.800	−10.160
Rx (s m^{-1})	−0.098	−0.661	+0.773	+0.682	+1.211
Rs (s m^{-1})	−5.23	−9.04	−15.72	−15.75	−19.28
T_{AC} (K)	*+1.09*	*+2.11*	*+2.70*	*+2.68*	*+2.61*

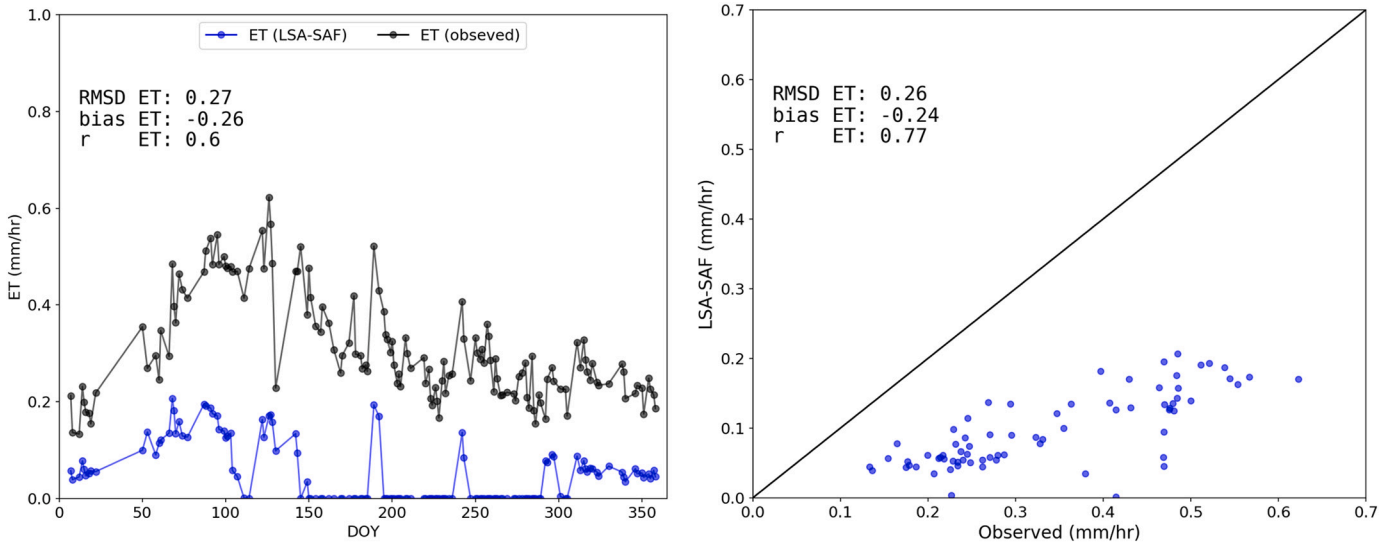

Fig. A4. Time series of LSA-SAF ET (mm/h) against average observed ET (mm/h) (left) and scatter plot of observed ET versus LSA-SAF ET (filtering for fluxes >0 mm/h) (right) for the year 2017.

The LSA-SAF ET product (Ghilain et al., 2011) were acquired for the same day and time of the Sen-ET images processed for 2017. The 30 min instantaneous ET product (in mm/h) were obtained and evaluated against the EC towers measurements of LE converted to ET (mm/h). The pixel unit is based on the SEVIRI instrument onboard the geostationary MSG satellite (roughly 3.7 km over the study site), therefore the average of all three EC tower ET measurements were used to evaluate the estimated ET.

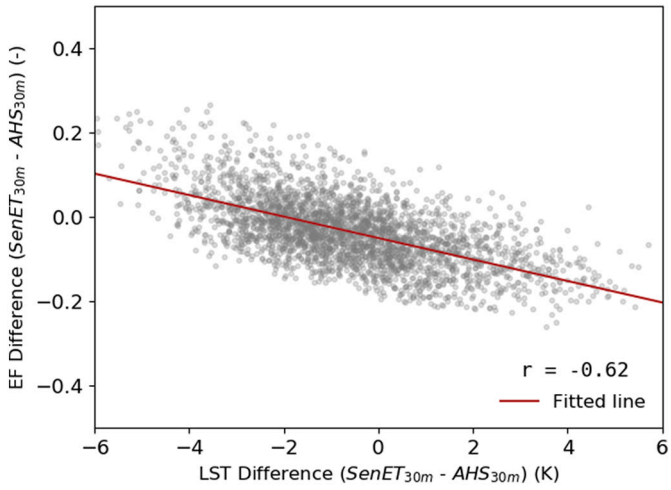

Fig. A5. Scatter plot of the difference in LST between Sentinel-3 sharpened LST (30 m) and AHS aggregated LST (30 m) versus the difference in EF Sen-ET_{30m} and AHS_{30m} for 2017-05-19.

Table A2
Summary statistics of the AHS aggregated LST (30 m) and Sentinel-3 sharpened LST (30 m) over the three tower footprint climatologies.

Tower footprint	*AHS-30 m (K)*			*S3–30 m (K)*			*Difference (K)*
	mean	*min*	*max*	*mean*	*min*	*max*	*mean*
CT	*309.18*	*304.70*	*312.91*	*308.25*	*307.31*	*309.31*	*−0.93*
NT	*308.26*	*304.27*	*311.26*	*306.83*	*305.96*	*307.82*	*−1.43*
NPT	*308.44*	*305.46*	*313.51*	*307.46*	*306.82*	*308.11*	*−0.98*

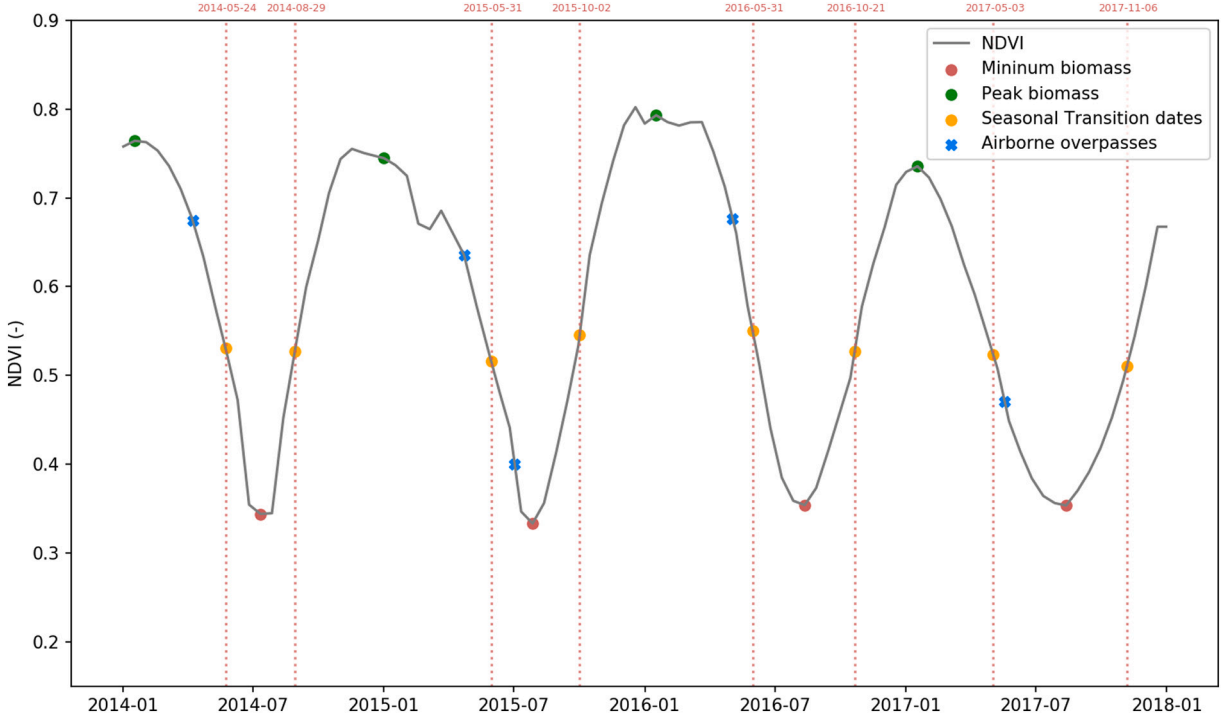

Fig. A6. Daily NDVI time series from the MODIS sensor (MCD43A4 product) over the CT tower between 2014 and 2017. Seasonal transition dates, as used in TSEB-2S, are shown in orange. Airborne overpass dates are highlighted in blue. (For interpretation of the references to colour in this figure legend, the reader is referred to the web version of this article.)

References

Ahlström, A., Raupach, M.R., Schurgers, G., Smith, B., Arneth, A., Jung, M., Reichstein, M., Canadell, J.G., Friedlingstein, P., Jain, A.K., 2015. The dominant role of semi-arid ecosystems in the trend and variability of the land CO2 sink. Science 348, 895–899.

Allard, V., Ourcival, J.M., Rambal, S., Joffre, R., Rocheteau, A., 2008. Seasonal and annual variation of carbon exchange in an evergreen Mediterranean forest in southern France. Glob. Chang. Biol. 14, 714–725. https://doi.org/10.1111/j.1365-2486.2008.01539.x.

Allen, R.G., Tasumi, M., Trezza, R., 2007. Satellite-based energy balance for mapping evapotranspiration with internalized calibration (METRIC)—model. J. Irrig. Drain. Eng. 133, 380–394. https://doi.org/10.1061/(ASCE)0733-9437(2007)133:4(380).

Anderson, M.C., Norman, J.M., Diak, G.R., Kustas, W.P., Mecikalski, J.R., 1997. A two-source time-integrated model for estimating surface fluxes using thermal infrared remote sensing. Remote Sens. Environ. 60, 195–216.

Anderson, M.C., Kustas, W.P., Norman, J.M., 2003. Upscaling and downscaling—a regional view of the soil–plant–atmosphere continuum. Agron. J. 95, 1408–1423. https://doi.org/10.2134/agronj2003.1408.

Anderson, M.C., Kustas, W.P., Norman, J.M., Hain, C.R., Mecikalski, J.R., Schultz, L., González-Dugo, M.P., Cammalleri, C., d'Urso, G., Pimstein, A., Gao, F., 2011. Mapping daily evapotranspiration at field to continental scales using geostationary and polar orbiting satellite imagery. Hydrol. Earth Syst. Sci. 15, 223–239. https://doi.org/10.5194/hess-15-223-2011.

Andreu, A., Kustas, W., Polo, M., Carrara, A., González-Dugo, M., 2018. Modeling surface energy fluxes over a Dehesa (Oak Savanna) ecosystem using a thermal based two source energy balance model (TSEB) II—integration of remote sensing medium and low spatial resolution satellite images. Remote Sens. 10, 558. https://doi.org/10.3390/rs10040558.

Bastiaanssen, W.G.M., Cheema, M.J.M., Immerzeel, W.W., Miltenburg, I.J., Pelgrum, H., 2012. Surface energy balance and actual evapotranspiration of the transboundary Indus Basin estimated from satellite measurements and the ETLook model. Water Resour. Res. 48.

Bellvert, J., Jofre-Ċekalović, C., Pelechá, A., Mata, M., Nieto, H., 2020. Feasibility of using the two-source energy balance model (TSEB) with sentinel-2 and sentinel-3 images to analyze the spatio-temporal variability of vine water status in a vineyard. Remote Sens. 12, 2299. https://doi.org/10.3390/rs12142299.

Biederman, J.A., Scott, R.L., Bell, T.W., Bowling, D.R., Dore, S., Garatuza-Payan, J., Kolb, T.E., Krishnan, P., Krofcheck, D.J., Litvak, M.E., Maurer, G.E., Meyers, T.P., Oechel, W.C., Papuga, S.A., Ponce-Campos, G.E., Rodriguez, J.C., Smith, W.K., Vargas, R., Watts, C.J., Yepez, E.A., Goulden, M.L., 2017. CO2 exchange and evapotranspiration across dryland ecosystems of southwestern North America. Glob. Chang. Biol. 23, 4204–4221. https://doi.org/10.1111/gcb.13686.

Bontemps, S., Defourny, P., Radoux, J., Van Bogaert, E., Lamarche, C., Achard, F., Mayaux, P., Boettcher, M., Brockmann, C., Kirches, G., 2013. Consistent global land cover maps for climate modelling communities: current achievements of the ESA's land cover CCI. In: Proceedings of the ESA Living Planet Symposium, Edimburgh, pp. 9–13.

Boulet, G., Mougenot, B., Lhomme, J.-P., Fanise, P., Lili-Chabaane, Z., Olioso, A., Bahir, M., Rivalland, V., Jarlan, L., Merlin, O., Coudert, B., Er-Raki, S., Lagouarde, J.-P., 2015. The SPARSE model for the prediction of water stress and evapotranspiration components from thermal infra-red data and its evaluation over irrigated and rainfed wheat. Hydrol. Earth Syst. Sci. 19, 4653–4672. https://doi.org/10.5194/hess-19-4653-2015.

Brunsell, N.A., Gillies, R.R., 2003. Scale issues in land–atmosphere interactions: implications for remote sensing of the surface energy balance. Agric. For. Meteorol. 117, 203–221. https://doi.org/10.1016/S0168-1923(03)00064-9.

Burchard-Levine, V., Nieto, H., Riaño, D., Migliavacca, M., El-Madany, T.S., Perez-Priego, O., Carrara, A., Martín, M.P., 2020. Seasonal adaptation of the thermal-based two-source energy balance model for estimating evapotranspiration in a semiarid tree-grass ecosystem. Remote Sens. 12, 904.

Campbell, G.S., Norman, J.M., 1998. An Introduction to Environmental Biophysics, 2nd edition. Springer-Verlag New York, New York.

Casals, P., Gimeno, C., Carrara, A., Lopez-Sangil, L., Sanz, Mj, 2009. Soil CO2 efflux and extractable organic carbon fractions under simulated precipitation events in a Mediterranean Dehesa. Soil Biol. Biochem. 41, 1915–1922. https://doi.org/10.1016/j.soilbio.2009.06.015.

Cleugh, H.A., Leuning, R., Mu, Q., Running, S.W., 2007. Regional evaporation estimates from flux tower and MODIS satellite data. Remote Sens. Environ. 106, 285–304.

Colaizzi, P.D., Evett, S.R., Howell, T.A., Tolk, J.A., 2004. Comparison of aerodynamic and radiometric surface temperature using precision weighing lysimeters. In: Remote Sensing and Modeling of Ecosystems for Sustainability. International Society for Optics and Photonics, pp. 215–230.

Coll, C., Caselles, V., Rubio, E., Sospedra, F., Valor, E., 2001. Temperature and emissivity separation from calibrated data of the digital airborne imaging spectrometer. Remote Sens. Environ. 76, 250–259.

Coll, C., Valor, E., Caselles, V., Niclòs, R., 2003. Adjusted Normalized Emissivity Method for surface temperature and emissivity retrieval from optical and thermal infrared remote sensing data. J. Geophys. Res.-Atmos. 108.

de Miguel, E., Jiménez, M., Pérez, I., Óscar, G., Muñoz, F., Gómez-Sánchez, J.A., 2015. AHS and CASI processing for the REFLEX remote sensing campaign: methods and results. Acta Geophys. 63, 1485–1498.

El-Madany, T.S., Reichstein, M., Perez-Priego, O., Carrara, A., Moreno, G., Pilar Martín, M., Pacheco-Labrador, J., Wohlfahrt, G., Nieto, H., Weber, U., Kolle, O., Luo, Y.-P., Carvalhais, N., Migliavacca, M., 2018. Drivers of spatio-temporal variability of carbon dioxide and energy fluxes in a Mediterranean savanna ecosystem. Agric. For. Meteorol. 262, 258–278. https://doi.org/10.1016/j.agrformet.2018.07.010.

El-Madany, T.S., Carrara, A., Martin, M.P., Moreno, G., Kolle, O., Pacheco-Labrador, J., Weber, T., Reichstein, M., Migliavacca, M., 2020. Drought and heatwave impacts on semi-arid ecosystems' carbon fluxes along a precipitation gradient. Philos. Trans. R. Soc. B. Biol. Sci. 375, 20190519. https://doi.org/10.1098/rstb.2019.0519.

Ershadi, A., McCabe, M.F., Evans, J.P., Walker, J.P., 2013. Effects of spatial aggregation on the multi-scale estimation of evapotranspiration. Remote Sens. Environ. 131, 51–62. https://doi.org/10.1016/j.rse.2012.12.007.

Fisher, J.B., Lee, B., Purdy, A.J., Halverson, G.H., Dohlen, M.B., Cawse-Nicholson, K., Wang, A., Anderson, R.G., Aragon, B., Arain, M.A., Baldocchi, D.D., Baker, J.M., Barral, H., Bernacchi, C.J., Bernhofer, C., Biraud, S.C., Bohrer, G., Brunsell, N., Cappelaere, B., Castro-Contreras, S., Chun, J., Conrad, B.J., Cremonese, E., Demarty, J., Desai, A.R., Ligne, A.D., Foltýnová, L., Goulden, M.L., Griffis, T.J., Grünwald, T., Johnson, M.S., Kang, M., Kelbe, D., Kowalska, N., Lim, J.-H., Maïnassara, I., McCabe, M.F., Missik, J.E.C., Mohanty, B.P., Moore, C.E., Morillas, L., Morrison, R., Munger, J.W., Posse, G., Richardson, A.D., Russell, E.S., Ryu, Y., Sanchez-Azofeifa, A., Schmidt, M., Schwartz, E., Sharp, I., Šigut, L., Tang, Y., Hulley, G., Anderson, M., Hain, C., French, A., Wood, E., Hook, S., 2020. ECOSTRESS: NASA's next generation mission to measure evapotranspiration from the international space station. Water Resour. Res. 56 https://doi.org/10.1029/2019WR026058 e2019WR02605.

Foken, T., 2017. Specifics of the near-surface turbulence. In: Foken, T. (Ed.), Micrometeorology. Springer, Berlin, Heidelberg, pp. 83–142. https://doi.org/10.1007/978-3-642-25440-6_3.

Foken, T., Aubinet, M., Finnigan, J.J., Leclerc, M.Y., Mauder, M., Paw, U., K., T., 2011. Results of a panel discussion about the energy balance closure correction for trace gases. Bull. Am. Meteorol. Soc. 92, ES13–ES18.

Friedl, M.A., Sulla-Menashe, D., Tan, B., Schneider, A., Ramankutty, N., Sibley, A., Huang, X., 2010. MODIS collection 5 global land cover: algorithm refinements and characterization of new datasets. Remote Sens. Environ. 114, 168–182.

Gao, F., Kustas, W.P., Anderson, M.C., 2012. A data mining approach for sharpening thermal satellite imagery over land. Remote Sens. 4, 3287.

Gastellu-Etchegorry, J.-P., Yin, T., Lauret, N., Cajgfinger, T., Gregoire, T., Grau, E., Feret, J.-B., Lopes, M., Guilleux, J., Dedieu, G., 2015. Discrete Anisotropic Radiative Transfer (DART 5) for modeling airborne and satellite spectroradiometer and LIDAR acquisitions of natural and urban landscapes. Remote Sens. 7, 1667–1701.

Gillies, R.R., Kustas, W.P., Humes, K.S., 1997. A verification of the "triangle" method for obtaining surface soil water content and energy fluxes from remote measurements of the Normalized Difference Vegetation Index (NDVI) and surface e. Int. J. Remote Sens. 18, 3145–3166. https://doi.org/10.1080/014311697217026.

Giri, C., Zhu, Z., Reed, B., 2005. A comparative analysis of the Global Land Cover 2000 and MODIS land cover data sets. Remote Sens. Environ. 94, 123–132. https://doi.org/10.1016/j.rse.2004.09.005.

Ghilain, N., Arboleda, A., Gellens-Meulenberghs, F., 2011. Evapotranspiration modelling at large scale using near-real time MSG SEVIRI derived data. Hydrol. Earth Syst. Sci. 15, 771–786. https://doi.org/10.5194/hess-15-771-2011.

Goudriaan, J., 1977. Crop Micrometeorology: A Simulation Stud. Center for Agricultural Publications and Documentation, Wageningen.

Guillevic, P.C., Bork-Unkelbach, A., Göttsche, F.M., Hulley, G., Gastellu-Etchegorry, J.-P., Olesen, F.S., Privette, J.L., 2013. Directional viewing effects on satellite land surface temperature products over sparse vegetation canopies—a multisensor analysis. IEEE Geosci. Remote Sens. Lett. 10, 1464–1468.

Guzinski, R., Nieto, H., 2019. Evaluating the feasibility of using Sentinel-2 and Sentinel-3 satellites for high-resolution evapotranspiration estimations. Remote Sens. Environ. 221, 157–172. https://doi.org/10.1016/j.rse.2018.11.019.

Guzinski, R., Nieto, H., Jensen, R., Mendiguren, G., 2014. Remotely sensed land-surface energy fluxes at sub-field scale in heterogeneous agricultural landscape and coniferous plantation. Biogeosciences 11, 5021–5046.

Guzinski, R., Nieto, H., El-Madany, T., Migliavacca, M., Carrara, A., 2018. Validation of fine resolution land-surface energy fluxes derived with combined sentinel-2 and sentinel-3 observations. In: IGARSS 2018–2018 IEEE International Geoscience and Remote Sensing Symposium. IEEE, pp. 8711–8714.

Guzinski, R., Nieto, H., Sandholt, I., Karamitilios, G., 2020. Modelling high-resolution actual evapotranspiration through sentinel-2 and sentinel-3 data fusion. Remote Sens. 12, 1433. https://doi.org/10.3390/rs12091433.

Hopwood, W.P., 1996. Observations and parametrization of momentum transfer in heterogeneous terrain consisting of regularly spaced obstacles. Boundary-Layer Meteorol. 81, 217–243. https://doi.org/10.1007/BF02430330.

Hu, G., Jia, L., 2015. Monitoring of evapotranspiration in a semi-arid inland river basin by combining microwave and optical remote sensing observations. Remote Sens. 7, 3056–3087.

Jia, L., 2004. Modeling Heat Exchanges at the Land-Atmosphere Interface Using Multi-Angular Thermal Infrared Measurements.

Jung, M., Reichstein, M., Bondeau, A., 2009. Towards Global Empirical Upscaling of FLUXNET Eddy Covariance Observations: Validation of a Model Tree Ensemble Approach Using a Biosphere Model.

Jung, M., Reichstein, M., Margolis, H.A., Cescatti, A., Richardson, A.D., Arain, M.A., Arneth, A., Bernhofer, C., Bonal, D., Chen, J., 2011. Global patterns of land-atmosphere fluxes of carbon dioxide, latent heat, and sensible heat derived from eddy covariance, satellite, and meteorological observations. J. Geophys. Res. Biogeosci. 116.

Jung, M., Koirala, S., Weber, U., Ichii, K., Gans, F., Camps-Valls, G., Papale, D., Schwalm, C., Tramontana, G., Reichstein, M., 2019. The FLUXCOM ensemble of global land-atmosphere energy fluxes. Sci. Data 6, 1–14. https://doi.org/10.1038/s41597-019-0076-8.

Kljun, N., Calanca, P., Rotach, M.W., Schmid, H.P., 2015. A simple two-dimensional parameterisation for Flux Footprint Prediction (FFP). Geosci. Model Dev. 8, 3695–3713. https://doi.org/10.5194/gmd-8-3695-2015.
Kondo, J., Ishida, S., 1997. Sensible heat flux from the earth's surface under natural convective conditions. J. Atmos. Sci. 54, 498–509.
Kustas, W.P., Anderson, M.C., 2009. Advances in thermal infrared remote sensing for land surface modeling. Agric. For. Meteorol. 149, 2071–2081.
Kustas, W.P., Norman, J.M., 1997. A two-source approach for estimating turbulent fluxes using multiple angle thermal infrared observations. Water Resour. Res. 33, 1495–1508. https://doi.org/10.1029/97WR00704.
Kustas, W.P., Norman, J.M., 1999. Evaluation of soil and vegetation heat flux predictions using a simple two-source model with radiometric temperatures for partial canopy cover. Agric. For. Meteorol. 94, 13–29.
Kustas, W.P., Norman, J.M., 2000. Evaluating the effects of subpixel heterogeneity on pixel average fluxes. Remote Sens. Environ. 74, 327–342. https://doi.org/10.1016/S0034-4257(99)00081-4.
Kustas, W., Li, F., Jackson, T., Prueger, J., MacPherson, J., Wolde, M., 2004. Effects of remote sensing pixel resolution on modeled energy flux variability of croplands in Iowa. Remote Sens. Environ. 92, 535–547.
Kustas, W.P., Alfieri, J.G., Anderson, M.C., Colaizzi, P.D., Prueger, J.H., Evett, S.R., Neale, C.M., French, A.N., Hipps, L.E., Chávez, J.L., 2012. Evaluating the two-source energy balance model using local thermal and surface flux observations in a strongly advective irrigated agricultural area. Adv. Water Resour. 50, 120–133.
Kustas, W.P., Nieto, H., Morillas, L., Anderson, M.C., Alfieri, J.G., Hipps, L.E., Villagarcía, L., Domingo, F., García, M., 2016. Revisiting the paper "Using radiometric surface temperature for surface energy flux estimation in Mediterranean drylands from a two-source perspective". Remote Sens. Environ. 184, 645–653.
Kustas, W.P., Alfieri, J.G., Nieto, H., Wilson, T.G., Gao, F., Anderson, M.C., 2019. Utility of the two-source energy balance (TSEB) model in vine and interrow flux partitioning over the growing season. Irrig. Sci. 37, 375–388. https://doi.org/10.1007/s00271-018-0586-8.
Lagouarde, J.-P., Commandoire, D., Irvine, M., Garrigou, D., 2013. Atmospheric boundary-layer turbulence induced surface temperature fluctuations. Implications for TIR remote sensing measurements. Remote Sens. Environ. 138, 189–198. https://doi.org/10.1016/j.rse.2013.06.011.
Lagouarde, J.-P., Irvine, M., Dupont, S., 2015. Atmospheric turbulence induced errors on measurements of surface temperature from space. Remote Sens. Environ. 168, 40–53. https://doi.org/10.1016/j.rse.2015.06.018.
Li, Y., Huang, C., Hou, J., Gu, J., Zhu, G., Li, X., 2017. Mapping daily evapotranspiration based on spatiotemporal fusion of ASTER and MODIS images over irrigated agricultural areas in the Heihe River Basin, Northwest China. Agric. For. Meteorol. 244–245, 82–97. https://doi.org/10.1016/j.agrformet.2017.05.023.
Li, Y., Kustas, W.P., Huang, C., Nieto, H., Haghighi, E., Anderson, M.C., Domingo, F., Garcia, M., Scott, R.L., 2019. Evaluating soil resistance formulations in thermal-based two-source energy balance (TSEB) model: implications for heterogeneous semiarid and arid regions. Water Resour. Res. 55, 1059–1078.
LICOR Bioscience USA, 2011. LAI-2200 Plant Canopy Analyzer. Instruction Manual. LICOR, Inc, Lincoln, NE. Available at. https://www.licor.com/env/support/LAI-2200C/manuals.html (accessed April 2021).
Luo, Y., El-Madany, T., Filippa, G., Ma, X., Ahrens, B., Carrara, A., Gonzalez-Cascon, R., Cremonese, E., Galvagno, M., Hammer, T., 2018. Using near-infrared-enabled digital repeat photography to track structural and physiological phenology in Mediterranean tree–grass ecosystems. Remote Sens. 10, 1293.
Ma, S., Baldocchi, D.D., Xu, L., Hehn, T., 2007. Inter-annual variability in carbon dioxide exchange of an oak/grass savanna and open grassland in California. Agric. For. Meteorol. 147, 157–171. https://doi.org/10.1016/j.agrformet.2007.07.008.
Ma, Y., Liu, S., Song, L., Xu, Z., Liu, Y., Xu, T., Zhu, Z., 2018. Estimation of daily evapotranspiration and irrigation water efficiency at a Landsat-like scale for an arid irrigation area using multi-source remote sensing data. Remote Sens. Environ. 216, 715–734.
Mahrt, L., EK, M., 1993. Spatial variability of turbulent fluxes and roughness lengths in HAPEX-MOBILHY. Boundary-Layer Meteorol. 65, 381–400. https://doi.org/10.1007/BF00707034.
Mahrt, L., 2000. Surface heterogeneity and vertical structure of the boundary layer. Bound.-Layer Meteorol. 96, 33–62.
Martens, B., Miralles, D.G., Lievens, H., van der Schalie, R., de Jeu, R.A.M., Fernández-Prieto, D., Beck, H.E., Dorigo, W.A., Verhoest, N.E.C., 2017. GLEAM v3: satellite-based land evaporation and root-zone soil moisture. Geosci. Model Dev. 10, 1903–1925. https://doi.org/10.5194/gmd-10-1903-2017.
McCabe, M.F., Wood, E.F., 2006. Scale influences on the remote estimation of evapotranspiration using multiple satellite sensors. Remote Sens. Environ. 105, 271–285.
McNaughton, K.G., Van Den Hurk, B.J.J.M., 1995. A "Lagrangian" revision of the resistors in the two-layer model for calculating the energy budget of a plant canopy. Bound.-Layer Meteorol. 74, 261–288.
Melendo-Vega, J.R., Martín, M.P., Pacheco-Labrador, J., González-Cascón, R., Moreno, G., Pérez, F., Migliavacca, M., García, M., North, P., Riaño, D., 2018. Improving the performance of 3-D radiative transfer model FLIGHT to simulate optical properties of a tree-grass ecosystem. Remote Sens. 10, 2061.
Mendiguren, G., Pilar Martín, M., Nieto, H., Pacheco-Labrador, J., Jurdao, S., 2015. Seasonal variation in grass water content estimated from proximal sensing and MODIS time series in a Mediterranean Fluxnet site. Biogeosciences 12, 5523–5535.
Migliavacca, M., Perez-Priego, O., Rossini, M., El-Madany, T.S., Moreno, G., van der Tol, C., Rascher, U., Berninger, A., Bessenbacher, V., Burkart, A., 2017. Plant functional traits and canopy structure control the relationship between photosynthetic CO 2 uptake and far-red sun-induced fluorescence in a Mediterranean grassland under different nutrient availability. New Phytol. 214, 1078–1091.
Moran, M.S., Humes, K.S., Pinter Jr., P.J., 1997. The scaling characteristics of remotely-sensed variables for sparsely-vegetated heterogeneous landscapes. J. Hydrol. 190, 337–362.
Moreno, G., Pulido, F.J., 2008. The functioning, management and persistence of Dehesas. In: Rigueiro-Rodróguez, A., McAdam, J., Mosquera-Losada, M.R. (Eds.), Agroforestry in Europe. Springer Netherlands, Dordrecht, pp. 127–160. https://doi.org/10.1007/978-1-4020-8272-6_7.
Mu, Q., Zhao, M., Running, S.W., 2011. Improvements to a MODIS global terrestrial evapotranspiration algorithm. Remote Sens. Environ. 115, 1781–1800. https://doi.org/10.1016/j.rse.2011.02.019.
Nassar, A., Torres-Rua, A., Kustas, W., Nieto, H., McKee, M., Hipps, L., Stevens, D., Alfieri, J., Prueger, J., Alsina, M.M., McKee, L., Coopmans, C., Sanchez, L., Dokoozlian, N., 2020. Influence of model grid size on the estimation of surface fluxes using the two source energy balance model and sUAS imagery in vineyards. Remote Sens. 12, 342. https://doi.org/10.3390/rs12030342.
Nieto, H., Kustas, W.P., Torres-Rúa, A., Alfieri, J.G., Gao, F., Anderson, M.C., White, W. A., Song, L., del Alsina, M.M., Prueger, J.H., McKee, M., Elarab, M., McKee, L.G., 2019. Evaluation of TSEB turbulent fluxes using different methods for the retrieval of soil and canopy component temperatures from UAV thermal and multispectral imagery. Irrig. Sci. 37, 389–406. https://doi.org/10.1007/s00271-018-0585-9.
Nishida, K., Nemani, R.R., Running, S.W., Glassy, J.M., 2003. An operational remote sensing algorithm of land surface evaporation. J. Geophys. Res.-Atmos. 108 https://doi.org/10.1029/2002JD002062.
Norman, J.M., Kustas, W.P., Humes, K.S., 1995. Source approach for estimating soil and vegetation energy fluxes in observations of directional radiometric surface temperature. Agric. For. Meteorol. 77, 263–293.
Norman, J., Anderson, M., Kustas, W., French, A., Mecikalski, J., Torn, R., Diak, G., Schmugge, T., Tanner, B., 2003. Remote sensing of surface energy fluxes at 101-m pixel resolutions. Water Resour. Res. 39.
Pacheco-Labrador, J., El-Madany, T.S., Martín, M.P., Migliavacca, M., Rossini, M., Carrara, A., Zarco-Tejada, P.J., 2017. Spatio-temporal relationships between optical information and carbon fluxes in a Mediterranean tree-grass ecosystem. Remote Sens. 9, 608. https://doi.org/10.3390/rs9060608.
Pacheco-Labrador, J., El-Madany, T.S., Martin, M.P., Gonzalez-Cascon, R., Carrara, A., Moreno, G., Perez-Priego, O., Hammer, T., Moossen, H., Henkel, K., Kolle, O., Martini, D., Burchard, V., van der Tol, C., Segl, K., Reichstein, M., Migliavacca, M., 2020. Combining hyperspectral remote sensing and eddy covariance data streams for estimation of vegetation functional traits (preprint). Biogeophysics. https://doi.org/10.5194/bg-2019-501.
Panofsky, H.A., 1984. Vertical variation of roughness length at the Boulder Atmospheric Observatory. Bound.-Layer Meteorol. 28, 305–308.
Perez-Priego, O., El-Madany, T.S., Migliavacca, M., Kowalski, A.S., Jung, M., Carrara, A., Kolle, O., Martín, M.P., Pacheco-Labrador, J., Moreno, G., Reichstein, M., 2017. Evaluation of eddy covariance latent heat fluxes with independent lysimeter and sapflow estimates in a Mediterranean savannah ecosystem. Agric. For. Meteorol. 236, 87–99. https://doi.org/10.1016/j.agrformet.2017.01.009.
Raupach, M.R., 1994. Simplified expressions for vegetation roughness length and zero-plane displacement as functions of canopy height and area index. Bound.-Layer Meteorol. 71, 211–216.
Richards, J.A., Jia, X., 2006. Remote Sensing Digital Image Analysis: An Introduction, 4th ed. Springer, Berlin.
Sauer, T.J., Norman, J.M., 1995. Simulated canopy microclimate using estimated below-canopy soil surface transfer coefficients. Agric. For. Meteorol. 75, 135–160.
Song, L., Liu, S., Kustas, W.P., Nieto, H., Sun, L., Xu, Z., Skaggs, T.H., Yang, Y., Ma, M., Xu, T., 2018. Monitoring and validating spatially and temporally continuous daily evaporation and transpiration at river basin scale. Remote Sens. Environ. 219, 72–88.
Stoy, P.C., Mauder, M., Foken, T., Marcolla, B., Boegh, E., Ibrom, A., Arain, M.A., Arneth, A., Aurela, M., Bernhofer, C., 2013. A data-driven analysis of energy balance closure across FLUXNET research sites: the role of landscape scale heterogeneity. Agric. For. Meteorol. 171, 137–152.
Su, Z., 2002. The Surface Energy Balance System (SEBS) for estimation of turbulent heat fluxes. Hydrol. Earth Syst. Sci. 6, 85–100. https://doi.org/10.5194/hess-6-85-2002.
Timmermans, W.J., Kustas, W.P., Anderson, M.C., French, A.N., 2007. An intercomparison of the Surface Energy Balance Algorithm for Land (SEBAL) and the Two-Source Energy Balance (TSEB) modeling schemes. Remote Sens. Environ. 108, 369–384. https://doi.org/10.1016/j.rse.2006.11.028.
Verhoef, A., De Bruin, H., Van Den Hurk, B., 1997. Some practical notes on the parameter kB- 1 for sparse vegetation. J. Appl. Meteorol. 36, 560–572.
Vihma, T., Savijärvi, H., 1991. On the effective roughness length for heterogeneous terrain. Q. J. R. Meteorol. Soc. 117, 399–407. https://doi.org/10.1002/qj.49711749808.
Whitley, R., Beringer, J., Hutley, L.B., Abramowitz, G., De Kauwe, M.G., Evans, B., Haverd, V., Li, L., Moore, C., Ryu, Y., Scheiter, S., Schymanski, S.J., Smith, B., Wang, Y.-P., Williams, M., Yu, Q., 2017. Challenges and opportunities in land surface modelling of savanna ecosystems. Biogeosciences 14, 4711–4732. https://doi.org/10.5194/bg-14-4711-2017.
Xu, T., He, X., Bateni, S.M., Auligne, T., Liu, S., Xu, Z., Zhou, J., Mao, K., 2019. Mapping regional turbulent heat fluxes via variational assimilation of land surface temperature data from polar orbiting satellites. Remote Sens. Environ. 221, 444–461.